Fermi National Accelerator Laboratory

FERMILAB Pub-94/072-E
CDF

Evidence for Color Coherence in $p\bar{p}$ Collisions at $\sqrt{s} = 1.8$ TeV

F. Abe et al
The CDF Collaboration

Fermi National Accelerator Laboratory, P.O. Box 500, Batavia, Illinois 60510

March 1994

Submitted to *Physical Review D*

Operated by Universities Research Association Inc. under Contract No. DE-AC02-76CHO3000 with the United States Department of Energy

Disclaimer

CDF/ANAL/JET/PUBLIC/2413
FERMILAB-PUB-94/072-E

Evidence for Color Coherence in $p\overline{p}$ Collisions at $\sqrt{s} = 1.8$ TeV

F. Abe,[12] M. Albrow,[6] D. Amidei,[15] C. Anway-Wiese,[3] G. Apollinari,[23] M. Atac,[6] P. Auchincloss,[22] P. Azzi,[17] N. Bacchetta,[16] A. R. Baden,[8] W. Badgett,[15] M. W. Bailey,[21] A. Bamberger,[6,a] P. de Barbaro,[22] A. Barbaro-Galtieri,[13] V. E. Barnes,[21] B. A. Barnett,[11] P. Bartalini,[20] G. Bauer,[14] T. Baumann,[8] F. Bedeschi,[20] S. Behrends,[2] S. Belforte,[20] G. Bellettini,[20] J. Bellinger,[28] D. Benjamin,[27] J. Benlloch,[14] J. Bensinger,[2] A. Beretvas,[6] J. P. Berge,[6] S. Bertolucci,[7] K. Biery,[10] S. Bhadra,[9] M. Binkley,[6] D. Bisello,[17] R. Blair,[1] C. Blocker,[2] A. Bodek,[22] V. Bolognesi,[20] A. W. Booth,[6] C. Boswell,[11] G. Brandenburg,[8] D. Brown,[8] E. Buckley-Geer,[6] H. S. Budd,[22] G. Busetto,[17] A. Byon-Wagner,[6] K. L. Byrum,[1] C. Campagnari,[6] M. Campbell,[15] A. Caner,[6] R. Carey,[8] W. Carithers,[13] D. Carlsmith,[28] J. T. Carroll,[6] R. Cashmore,[6,a] A. Castro,[17] Y. Cen,[18] F. Cervelli,[20] K. Chadwick,[6] J. Chapman,[15] G. Chiarelli,[7] W. Chinowsky,[13] S. Cihangir,[6] A. G. Clark,[6] M. Cobal,[20] D. Connor,[18] M. Contreras,[4] J. Cooper,[6] M. Cordelli,[7] D. Crane,[6] J. D. Cunningham,[2] C. Day,[6] F. DeJongh,[6] S. Dell'Agnello,[20] M. Dell'Orso,[20] L. Demortier,[23] B. Denby,[6] P. F. Derwent,[15] T. Devlin,[24] M. Dickson,[22] S. Donati,[20] R. B. Drucker,[13] A. Dunn,[15] K. Einsweiler,[13] J. E. Elias,[6] R. Ely,[13] S. Eno,[4] S. Errede,[9] A. Etchegoyen,[6,a] B. Farhat,[14] M. Frautschi,[16] G. J. Feldman,[8] B. Flaugher,[6] G. W. Foster,[6] M. Franklin,[8] J. Freeman,[6] H. Frisch,[4] T. Fuess,[6] Y. Fukui,[12] G. Gagliardi,[20] A. F. Garfinkel,[21] A. Gauthier,[9] S. Geer,[6] D. W. Gerdes,[15] P. Giannetti,[20] N. Giokaris,[23] P. Giromini,[7] L. Gladney,[18] M. Gold,[16] J. Gonzalez,[18] K. Goulianos,[23] H. Grassmann,[17] G. M. Grieco,[20] R. Grindley,[10] C. Grosso-Pilcher,[4] C. Haber,[13]

Submitted to Phys. Rev. D March 22, 1994

S. R. Hahn,[6] R. Handler,[28] K. Hara,[26] B. Harral,[18] R. M. Harris,[6] S. A. Hauger,[5] J. Hauser,[3] C. Hawk,[24] T. Hessing,[25] R. Hollebeek,[18] A. Hölscher,[10] S. Hong,[15] G. Houk,[18] P. Hu,[19] B. Hubbard,[13] B. T. Huffman,[19] R. Hughes,[22] P. Hurst,[8] J. Huth,[6] J. Hylen,[6] M. Incagli,[20] T. Ino,[26] H. Iso,[26] H. Jensen,[6] C. P. Jessop,[8] R. P. Johnson,[6] U. Joshi,[6] R. W. Kadel,[13] T. Kamon,[25] S. Kanda,[26] D. A. Kardelis,[9] I. Karliner,[9] E. Kearns,[8] L. Keeble,[25] R. Kephart,[6] P. Kesten,[2] R. M. Keup,[9] H. Keutelian,[6] D. Kim,[6] S. B. Kim,[15] S. H. Kim,[26] Y. K. Kim,[13] L. Kirsch,[2] K. Kondo,[26] J. Konigsberg,[8] K. Kordas,[10] E. Kovacs,[6] M. Krasberg,[15] S. E. Kuhlmann,[1] E. Kuns,[24] A. T. Laasanen,[21] S. Lammel,[3] J. I. Lamoureux,[28] S. Leone,[20] J. D. Lewis,[6] W. Li,[1] P. Limon,[6] M. Lindgren,[3] T. M. Liss,[9] N. Lockyer,[18] M. Loreti,[17] E. H. Low,[18] D. Lucchesi,[20] C. B. Luchini,[9] P. Lukens,[6] P. Maas,[28] K. Maeshima,[6] M. Mangano,[20] J. P. Marriner,[6] M. Mariotti,[20] R. Markeloff,[28] L. A. Markosky,[28] J. A. J. Matthews,[16] R. Mattingly,[2] P. McIntyre,[25] A. Menzione,[20] E. Meschi,[20] T. Meyer,[25] S. Mikamo,[12] M. Miller,[4] T. Mimashi,[26] S. Miscetti,[7] M. Mishina,[12] S. Miyashita,[26] Y. Morita,[26] S. Moulding,[23] J. Mueller,[24] A. Mukherjee,[6] T. Muller,[3] L. F. Nakae,[2] I. Nakano,[26] C. Nelson,[6] D. Neuberger,[3] C. Newman-Holmes,[6] J. S. T. Ng,[8] M. Ninomiya,[26] L. Nodulman,[1] S. Ogawa,[26] C. Pagliarone,[20] R. Paoletti,[20] V. Papadimitriou,[6] A. Para,[6] E. Pare,[8] S. Park,[6] J. Patrick,[6] G. Pauletta,[20] L. Pescara,[17] T. J. Phillips,[5] A. G. Piacentino,[20] R. Plunkett,[6] L. Pondrom,[28] J. Proudfoot,[1] F. Ptohos,[8] G. Punzi,[20] D. Quarrie,[6] K. Ragan,[10] G. Redlinger,[4] J. Rhoades,[28] M. Roach,[27] F. Rimondi,[6,a] L. Ristori,[20] W. J. Robertson,[5] T. Rodrigo,[6] T. Rohaly,[18] A. Roodman,[4] W. K. Sakumoto,[22] A. Sansoni,[7] R. D. Sard,[9] A. Savoy-Navarro,[6] V. Scarpine,[9] P. Schlabach,[8], E. E. Schmidt,[6] O. Schneider,[13] M. H. Schub,[21] R. Schwitters,[8] G. Sciacca,[20] A. Scribano,[20] S. Segler,[6] S. Seidel,[16] Y. Seiya,[26] G. Sganos,[10]

M. Shapiro,[13] N. M. Shaw,[21] M. Sheaff,[28] M. Shochet,[4] J. Siegrist,[13] A. Sill,[22] P. Sinervo,[10] J. Skarha,[11] K. Sliwa,[27] D. A. Smith,[20] F. D. Snider,[11] L. Song,[6] T. Song,[15] M. Spahn,[13] P. Sphicas,[14] A. Spies,[11] R. St. Denis,[8] L. Stanco,[17] A. Stefanini,[20] G. Sullivan,[4] K. Sumorok,[14] R. L. Swartz, Jr.,[9] M. Takano,[26] K. Takikawa,[26] S. Tarem,[2] F. Tartarelli,[20] S. Tether,[14] D. Theriot,[6] M. Timko,[27] P. Tipton,[22] S. Tkaczyk,[6] A. Tollestrup,[6] J. Tonnison,[21] W. Trischuk,[8] Y. Tsay,[4] J. Tseng,[11] N. Turini,[20] F. Ukegawa,[26] D. Underwood,[1] S. Vejcik, III,[15] R. Vidal,[6] R. G. Wagner,[1] R. L. Wagner,[6] N. Wainer,[6] R. C. Walker,[22] J. Walsh,[18] A. Warburton,[10] G. Watts,[22] T. Watts,[24] R. Webb,[25] C. Wendt,[28] H. Wenzel,[20] W. C. Wester, III,[13] T. Westhusing,[9] S. N. White,[23] A. B. Wicklund,[1] E. Wicklund,[6] H. H. Williams,[18] B. L. Winer,[22] J. Wolinski,[25] D. Y. Wu,[15] X. Wu,[20] J. Wyss,[17] A. Yagil,[6] W. Yao,[13] K. Yasuoka,[26] Y. Ye,[10] G. P. Yeh,[6] J. Yoh,[6] M. Yokoyama,[26] J. C. Yun,[6] A. Zanetti,[20] F. Zetti,[20] S. Zhang,[15] W. Zhang,[18] S. Zucchelli,[6,a]

The CDF Collaboration

[1] *Argonne National Laboratory, Argonne, Illinois 60439*

[2] *Brandeis University, Waltham, Massachusetts 02254*

[3] *University of California at Los Angeles, Los Angeles, California 90024*

[4] *University of Chicago, Chicago, Illinois 60637*

[5] *Duke University, Durham, North Carolina 27706*

[6] *Fermi National Accelerator Laboratory, Batavia, Illinois 60510*

[7] *Laboratori Nazionali di Frascati, Istituto Nazionale di Fisica Nucleare, Frascati, Italy*

[8] *Harvard University, Cambridge, Massachusetts 02138*

[9] *University of Illinois, Urbana, Illinois 61801*

[10] *Institute of Particle Physics, McGill University, Montreal, and University of Toronto, Toronto, Canada*

[11] *The Johns Hopkins University, Baltimore, Maryland 21218*

[12] *National Laboratory for High Energy Physics (KEK), Japan*

[13] *Lawrence Berkeley Laboratory, Berkeley, California 94720*

[14] *Massachusetts Institute of Technology, Cambridge, Massachusetts 02139*

[15] *University of Michigan, Ann Arbor, Michigan 48109*

[16] *University of New Mexico, Albuquerque, New Mexico 87131*

[17] *Universita di Padova, Instituto Nazionale di Fisica Nucleare, Sezione di Padova, I-35131 Padova, Italy*

[18] *University of Pennsylvania, Philadelphia, Pennsylvania 19104*

[19] *University of Pittsburgh, Pittsburgh, Pennsylvania 15260*

[20] *Istituto Nazionale di Fisica Nucleare, University and Scuola Normale Superiore of Pisa, I-56100 Pisa, Italy*

[21] *Purdue University, West Lafayette, Indiana 47907*

[22] *University of Rochester, Rochester, New York 15627*

[23] *Rockefeller University, New York, New York 10021*

[24] *Rutgers University, Piscataway, New Jersey 08854*

[25] *Texas A&M University, College Station, Texas 77843*

[26] *University of Tsukuba, Tsukuba, Ibaraki 305, Japan*

[27] *Tufts University, Medford, Massachusetts 02155*

[28] *University of Wisconsin, Madison, Wisconsin 53706*

Abstract

Color coherence effects in $p\overline{p}$ collisions are observed and studied with CDF, the Collider Detector at the Fermilab Tevatron collider. We demonstrate these effects by measuring spatial correlations between soft and leading jets in multi jet events. Variables sensitive to interference are identified by comparing the data to the predictions of various shower Monte Carlos that are substantially different with respect to the implementation of coherence.

PACS numbers: 13.87.-a, 12.38.Qk, 13.85.-t, 13.90.+i

I. INTRODUCTION

Color coherence phenomena have been clearly observed in e^+e^- collisions [1, 2] and thoroughly examined from a theoretical point of view [3]. Owing to difficulties in detecting unambiguous effects in the data, however, we still lack significant experimental checks in $p\overline{p}$ collisions. Here, we report the first direct evidence for such effects observed in a hadron collider experiment, using 4.2 pb^{-1} of data collected by the Collider Detector at Fermilab (CDF) during the 1988-89 run of the Tevatron collider.

These color coherence studies provide several important tests of QCD [4, 5] and of the way in which QCD is implemented in the current theoretical calculations. The measurement of emission patterns for gluon radiation provides tests of perturbative QCD beyond the leading order in perturbation theory. This measurement can also help to unravel the interplay between the perturbative and the non-perturbative regimes. The importance of this goal resides in the fact that the perturbative evolution is well described and interpreted in terms of first principles, whilst the non-perturbative regime is described only by phenomenological models. For a full exploitation of the strong predictive power of the perturbative approach, it is essential to understand which features of the perturbative partonic evolution are preserved through the non-perturbative hadronization process and which are not. This knowledge can only be derived from experimental tests.

From an experimental point of view, a deeper understanding of the radiation structure in hard processes should help to distinguish events generated by exotic phenomena from those generated by standard QCD interactions. It is therefore important to assess experimentally which of the distinguishing features expected from theoretical calculations survive the smearing induced by detector effects and the presence of the underlying event, namely the soft particles produced by the collision between the fragments of the initial state hadrons.

The most striking consequence of color coherence phenomena in QCD is given by the inhibition of soft radiation emission [6]. One way in which this interference manifests itself, is the so called *string effect* [1, 2, 3], whereby the amount of soft radiation emitted in the region between the two quark jets in a $e^+e^- \rightarrow$ 3-jet event is suppressed with respect to the region between the quark and the gluon jets. This effect is understood as the result of destructive interference between amplitudes with soft gluons emitted by color connected partons. Fig. 1 serves to clarify this point. The lines connecting the two quarks with the gluon represent the flow of the color charges involved in the process, and can be identified as antennas for the emission of additional color radiation. QCD predicts that these antennas behave approximately like standard dipoles, and therefore the radiation is concentrated mainly in the two regions towards which the antennas are pointing.

Similar graphs can be obtained for any QCD hard process, in particular for hadronic collisions where initial state colored partons are involved. Depending on the details of the hard scattering, different color flows are involved, and several color patterns can contribute to the same process. The multitude of possible color flows participating in a hadronic process makes it very hard to identify a characteristic emission pattern. Until now, this has been one of the two major obstacles in obtaining compelling experimental evidence for these phenomena. The other obstacle that has prevented the identification of a clear signal is the difficulty of separating the contribution of soft particles produced by the underlying event: whilst these are expected to be distributed, on average, isotropically in azimuth (ϕ) and pseudorapidity ($\eta = -\log(tan\theta/2)$), event by event fluctuations in their distributions will bias any attempt to identify intrinsic asymmetries of the soft radiation produced in the hard scattering.

In this article, we show how it is possible to overcome both of these difficulties. We use the high energies available at the Tevatron to select events where the energy of the leading jets is so large that soft radiation is hard enough to form secondary jets. The spatial correlations between these secondary jets and the leading ones will give us variables similar to those used in the study of the string effect in e^+e^- collisions. A systematic comparison of the results with the predictions of some of the available theoretical calculations based on shower Monte Carlo generators will give evidence that what we are observing is indeed the result of color coherence. Preliminary results of this analysis have already been reported [7]. Preliminary results have also been presented recently by the D0 collaboration [8].

The outline of the paper is as follows: in Sec. II we cover in more detail the physics ideas underlying this measurement; we review the way different theoretical calculations incorporate these ideas and introduce the variables that will be used in the present analysis. In Sec. III we present the components of the CDF detector which are relevant to this study and describe the triggers and the data selection criteria. Here we will also describe the generation of the Monte Carlo samples used for the comparison of the data with the theoretical expectations. In Sec. IV we present and compare the data to the Monte Carlo results. In Sec. V we report the study of the experimental systematics. In Sec. VI we present a thorough discussion of the results, a comparison among the predictions of the different Monte Carlo programs and a complete evaluation of the impact of different approximation schemes. In Sec. VII, finally, we report the conclusions.

II. CONSTRUCTION OF VARIABLES SENSITIVE TO COHERENCE

As mentioned in the Introduction, color coherence leads to a suppression of soft gluon radiation in certain regions of phase space. Theoretical studies [6] show that these effects can be implemented in a shower Monte Carlo evolution by properly constraining the phase space allowed for the emission. In the case of final state showers (time-like evolution), this is achieved by requiring the emission angle in subsequent branchings to be decreasing and the radiation to be limited to lie within cones defined by color flow lines. This prescription is shown in Fig. 2, and is known as angular ordering.

Final state coherence is included in the shower Monte Carlos HERWIG [10] and PYTHIA [11], but is absent in ISAJET [12]. Monte Carlo programs including coherence via angular ordering in final state cascades have been extensively and successfully used to describe features of the experimental data in e^+e^-experiments [1, 2].

The phase space constraint in the case of radiation from an incoming initial state parton (space-like evolution) is slightly more complicated [13], but still amounts qualitatively to an angular ordering, with emission angles increasing as one moves from the initial hadron to the hard subprocess. A memory is retained of the shower initiator direction, even after many branchings. So far, HERWIG is the only program to fully include this kind of coherence.

In addition to constraining the independent evolutions of space-like and time-like showers, color coherence gives a prescription for the emission of the first gluon from initial and final state partons [10, 14]. This prescription is required in order to provide the correct boundary conditions for the evolution of the initial and final states. We will consider as an example the case of 2 → 2 scattering. Each contributing process is decomposed into the various possible color flow configurations. In the approximation that neglects suppressed interference terms [9, 10, 14], all of the color configurations for the 2 → 2 process add incoherently to the total scattering probability. Then, each color configuration defines radiation cones in which partons can emit, following the angular ordering constraint defined for time-like showers. An explicit example is given in Fig. 3. In this particular example, the color lines flow from the initial to the final state partons, creating asymmetries in the structure of the observed soft radiation that are unique to collisions involving hadrons in both the initial and final states. These initial-final state color interference effects cannot be found in e^+e^- reactions, and have not been observed so far. PYTHIA includes these interference effects at the non-perturbative level via string fragmentation, but only HERWIG takes them into account within the perturbative evolution.

In this study, we intend to concentrate on observables which emphasize these initial-final state coherence effects and which allow us to disentangle them from the more standard final state coherence, already observed and tested in e^+e^- physics.

Several measurements have been suggested in the past to observe this phenomenon, most notably the study of radiation patterns in events where a prompt photon is produced in association with a high P_T jet [3]. In this class of events, in fact, the final state jet is always color connected to either of the two initial state partons, therefore creating the conditions for initial-final state coherence. Fluctuations in the underlying event, however, will make the detection of soft radiation asymmetries very difficult. To overcome this problem, we consider events where the soft radiation is hard enough to be reconstructed as a jet. The probability that jets be formed by fluctuations of the underlying event is very small, and therefore the measurement of coherence effects becomes possible.

In order for the coherence phenomena to manifest themselves, it is necessary that the energy of the emitted gluons be small relative to the energy of the emitters. This requires events where the leading jets have energies in excess of 100 GeV, so that emitted jets with P_T above 10 GeV may be considered as soft. In order to collect sufficient statistics, we are then forced to study QCD dijet events, as the cross section for production of prompt photons above 100 GeV is too small.

Now, let us identify the variables that we expect to be sensitive to interference effects. Consider Fig. 4, which shows the spatial distribution of radiation for the hard $2 \rightarrow 2$ scattering displayed in Fig. 3. In this example, the emitting antenna is the line connecting partons 1 and 2. We define regions A and B, respectively, as the allowed emission cones for parton 1 and 2 as defined by the angular ordering prescription. The two cones overlap in region C, which is therefore a region of unsuppressed radiation.

In the region complementary to A and B the soft emission is forbidden.

Smaller scattering angles, θ_s, correspond to tighter phase space constraints. Our ignorance of the color topology prevents us from unequivocally determining the restriction cones for each observed event. Therefore, the aim is to identify variables that preserve some amount of the statistical correlations introduced by the restriction cones. Notice that, because of transverse momentum conservation, if the gluon forming the additional jet is emitted in region B, the jet recoiling against parton 2 will become the leading-E_T jet of the event. Parton 2 and the emitted gluon will, therefore, most often form the second- and third-E_T jets of the event. This suggests considering correlations between the directions of the second and third jet in the event.

We will measure the spatial distribution of the third jet around the second one using the distance in pseudorapidity, $\Delta\eta = \eta_3 - \eta_2$, and the distance in the azimuthal angle, $\Delta\phi = \phi_3 - \phi_2$. In order to better single out the region of maximum emission, we introduce the variable $\Delta H = sign(\eta_2) * \Delta\eta$. $\Delta H > 0$ corresponds to the region A in the example of Fig. 4.

Fig. 5 shows the density of the third-E_T jets in the $(|\Delta\phi|, \Delta H)$ space for the data sample to be defined in the next section. The azimuthal distance $|\Delta\phi|$, shown on the horizontal axis, spans the range $[0, \pi]$, whereas, ΔH, shown on the vertical axis, is constrained by the calorimeter acceptance to be in the range $|\Delta H| < 4$. For each event, the second jet is located at the origin, while the first jet is expected to be more or less back to back in ϕ, that is near the edge $|\Delta\phi| = \pi$. The position of the third jet axis is represented by a point in the plane.

Since the jets have been reconstructed using a fixed-cone clustering algorithm

[15, 16] with cone radius $R_{cone} = 0.7$, the circular region of radius R_{cone} in the $(|\Delta\phi|, \Delta H)$ space around the second jet axis is forbidden to other jets. Therefore, a set of "polar" variables turns out to be useful. We define $R = \sqrt{(\Delta\eta^2 + \Delta\phi^2)}$ and $\alpha = atan(\Delta H/|\Delta\phi|)$ as our variables of choice. The variable R is the distance between the third and second jet in the (η, ϕ) space. The variable α is the polar angle in the $(|\Delta\phi|, \Delta H)$ space.

In Fig. 6 the regions A, B, and C of Fig. 4 are mapped on the (α, R) space. The black region on top is forbidden by the limit $|\Delta\phi| < \pi$, while the straight line at $R = R_{cone} = 0.7$ shows the boundary around the second jet axis, generated by the clustering algorithm. The figure illustrates the boundaries imposed by the angular ordering restriction for the case of $\theta_s = 85°$. We then expect the distributions of variables such as α and R to be sensitive to the phase space constraints imposed by the color interference.

In conclusion, we plan to use the α and R variables to exhibit color coherence. We will also study the absolute pseudorapidity of the third jet, η_3. Color coherence is expected to broaden the η_3 distribution, increasing the probability of having third jets at large pseudorapidities. This is because the coherent emission "remembers" the first prong of the radiating antenna, that is, the beam line.

III. THE APPARATUS, THE DATA AND THE MONTE CARLO SAMPLES

A. The Apparatus

The CDF detector has been described in detail elsewhere [17]; here we briefly review the components relevant to this analysis. A side-view cross section of the

CDF detector is shown in Fig. 7.

Scintillator planes located at small angles with respect to the beam directions are used to tag inelastic events. A vertex time-projection chamber (VTPC) provides r-z tracking information for $|\eta| < 3.5$. This chamber is used to measure the position of the interaction vertex along the beam axis with a resolution of 1 mm. At larger radii, an 84-layer central tracking chamber (CTC) measures charged-particle momenta for $|\eta| < 1.2$ in a 1.4 T magnetic field with a precision of $\delta p_T/p_T^2 = 0.0011\ (GeV/c)^{-1}$ for beam constrained tracks [18].

Outside the tracking chambers, electromagnetic and hadronic calorimeters are arranged in a fine-grained, projective tower geometry covering most of the 4π solid angle. The calorimeters are divided into three regions of pseudorapidity: central, plug, and forward. The central electromagnetic (CEM) and hadronic (CHA) calorimeters consist of lead- and iron-scintillator sandwiches, respectively. The coverage of the central hadronic calorimeter is completed by the iron-scintillator End Wall (WHA) calorimeter in the transition region $0.7 < |\eta| < 1.3$ (Fig. 7). In the plug and forward regions, the calorimeters are constructed with gas proportional chambers. PEM (PHA), and FEM (FHA) stand for plug, and forward electromagnetic (hadronic). The segmentation of the calorimeters is $\Delta\eta \times \Delta\phi = 0.1 \times 15^o$ in the central region and $\Delta\eta \times \Delta\phi = 0.1 \times 5^o$ in the plug and forward regions. The calorimeter systems are summarized in Table 1.

B. The Data Sample

The data were collected using a single-jet online trigger, which required at least one cluster of transverse energy $E_t = Esin\theta$ greater than a threshold of 60 GeV.

The uncorrected energy of a jet is defined by the clustering algorithm [16] as the scalar sum of the measured energies in the electromagnetic and hadronic compartments within a cone around the cluster centroid. The momentum of the cluster is calculated by assuming that the energy in each calorimeter tower belonging to the cluster is deposited by a massless particle hitting the center of the tower.

The measured energy and momentum of each jet are corrected, on average, for detector effects: degradation of the measurement due to calorimeter non-linearity, uninstrumented regions of the detector and bending of charged particle tracks in the CDF 1.4 T solenoid magnetic field in the central region. The absolute energy response is derived [19] from Monte Carlo jets generated in the central region and processed through a full detector simulation. The average energy degradation is 17% (12%) at 35 (300) GeV. The Monte Carlo program is tuned to reproduce (a) the charged particle fragmentation of jets observed in the data and (b) the calorimeter response to single charged pions and electrons (measured in a test beam) and to single isolated charged particles in the data from $p\overline{p}$ collisions. The true jet energy (E) and momentum ($\mathbf{p}$) are defined as the total energy and momentum of all the particles (leptons, photons, and hadrons) emerging from the primary vertex within a cone of fixed radius R_{cone} around the cluster centroid. No attempt is made to reconstruct the energy of the parton from which the jet originates, e.g. no corrections are applied to account for energy lost out of the clustering cone or to account for the underlying event. Our energy scale corrections are intended to produce an unbiased estimate of the true jet 4-momentum $(E, \mathbf{p})$, defined above. To measure the relative response of the detectors at large pseudorapidity, jet p_T balancing is used. The method is fully described in references [19], [20].

The cosmic ray background is rejected with criteria described in reference [21].

Events with a significant missing transverse energy are rejected if one of the two leading jets has an electromagnetic fraction smaller than 0.05 or greater than 0.95. The missing transverse energy significance is calculated as $(MET)^2 = [(\Sigma E_T sin\phi)^2 + (\Sigma E_T cos\phi)^2]/(\Sigma E_T)$, with E_T measured in GeV, and is required to satisfy $MET > 6$. The E_T-sums include only the energy that has been clustered into jets.

The criteria for the event selection are listed below.

1. The event vertex along the beam line is required to be within 60 cm of the center of the detector.

2. The two leading jet axes (i.e., those with the highest transverse energies) are required to be in the pseudorapidity ranges $|\eta_1|, |\eta_2| < 0.7$. This ensures that the two leading jet cores are well contained in the central calorimeter.

3. $||\phi_1 - \phi_2| - \pi| < 20^o$; the two leading jets are required to be back to back within 20^o in the transverse plane. This is a loose cut to select events with soft radiation, which are well described in the approximation of the shower Monte Carlos.

4. The measured transverse energy of the first jet in the event, E_{T1}, is required to be large enough such that it is free of biases introduced by the trigger threshold. The corrected E_{T1} threshold above which our data selection is fully efficient is 110 GeV. This 100% efficiency point is measured through the use of lower trigger threshold data.

5. The presence of a third jet is required. In order to avoid the possible background due to underlying event fluctuations, the third jet corrected transverse energy, E_{T3}, is required to be greater than 10 GeV.

6. This last selection requirement is applied only for the study of the α variable: a rectangular region of uniform acceptance in the scatter plot α versus R (Fig. 6) is chosen by requiring that $1.1 < R < \pi$. The former condition removes the sharp rise due to the clustering algorithm, whilst the latter condition discards the upper region of the α dependent acceptance.

C. The Simulated Samples

We use different shower Monte Carlos to generate jet events that are subsequently processed by the CDF detector simulator.

The Monte Carlo HERWIG (version 3.2) imposes proper phase space constraints on soft emissions from any kind of color antenna, including those spanned between the initial and final states (initial-final state antenna).

The Monte Carlo ISAJET (version 6.25) does not implement angular ordering in the initial or the final state radiation.

The Monte Carlo PYTHIA (version 5.6) imposes proper phase space constraints only on soft emissions of time-like shower evolutions. In particular, this does not include initial-final state antennas. PYTHIA was written when theoretical results pertaining to coherence were available only for the time-like shower evolution, and does not implement the more complicated angular ordering of the space-like shower evolution. This approximation is appropriate for describing e^+e^-results, or for studying W/Z events in $p\overline{p}$ collisions, where there is no interference between initial and final state.

Since we intend to concentrate on initial-final state color interference effects, we also use a new version of PYTHIA, expressly provided by the author T. Sjöstrand, which implements the phase space constraints for the initial-final state antennas [22] as well. This version will be called PYTHIA+ [1].

PYTHIA has a feature that allows one to switch on and off the simulation of color coherence, without altering any other feature of the event generation. We have generated a sample of PYTHIA events with no simulation of color coherence (PYTHIA-off).

We have generated all the samples with transverse momenta p_T of the final state partons greater than 75 GeV. Since our analysis involves only central leading jets, we have constrained the final state partons to lie in the rapidity interval $|y| < 1.5$, hence achieving high statistics with the least CPU-time. Control samples, with a smaller p_T threshold and a greater rapidity interval, have been generated to check for the absence of biases introduced by the above generation cuts in the selected samples.

In addition to the standard CDF simulation, we have also processed the generated events through a fast simulation of an ideal calorimeter where the particle's energy is exactly measured. The tower segmentation of the ideal calorimeter is the same of the real one, but with no dead regions. The output of the fast simulation is then processed by the standard clustering algorithm, that in this case defines precisely "measured" jets. The primary vertex is always at the center of the detector and no magnetic field is simulated.

We have generated 280000 events for each sample, corresponding to the integrated luminosities listed in Table 2. This table also lists the number of events in the samples after the different selection cuts.

---

[1] These modifications are now implemented in the latest version of PYTHIA, 5.7

IV. COLOR COHERENCE IN THE DATA

In order to exhibit the color coherence effects, we compare the data to the predictions of the different shower Monte Carlos. Unless otherwise specified, all of the distributions presented in this paper represent probabilities and are normalized to unit area; i.e., only the shapes of the distributions are compared. The distributions are uncorrected for detector effects, such as finite resolution smearing and uninstrumented regions; these effects are included in the detector simulation. The error bars shown on the data points are statistical errors only. The main systematics are discussed in Sec. V, and are shown to be small.

For each Monte Carlo sample we first check that the distributions for the pseudorapidities and transverse energies of the two leading jets are in good agreement with the data. This gives us confidence that the main hard scattering features are reproduced by all the physics generators. In order to illustrate the typical level of agreement between data and all of the Monte Carlos, we show in Figs. 8 and 9, the comparison between the transverse energy distributions for the real and the simulated data.

In direct contrast, the distributions of variables sensitive to interference exhibit differences between the different Monte Carlos. Fig. 10 shows the third jet pseudorapidity (η_3) distributions for HERWIG (a), ISAJET (b), PYTHIA (c), and PYTHIA+ (d), superimposed on the data. Local distortions of the shape, such as those at $|\eta_3| = 2.5$, are due to uninstrumented regions of the detector that modulate the efficiency as a function of η_3. The distributions of HERWIG and PYTHIA+ agree better with the data than those of ISAJET and PYTHIA, which are narrower and have a clear excess of events at small η.

Figs. 11 and 12 show similar comparisons for the variables R and α defined in Sec. II. Again, HERWIG (a) and PYTHIA+ (d) reproduce the data better than ISAJET (b) and PYTHIA (c). The coherence effect in Fig. 12 is observable as a change of slope for $\alpha \to \pi/2$. This change is present in the data, HERWIG and PYTHIA+ distributions. The ISAJET and PYTHIA distributions, instead, are monotonically decreasing from $\alpha = -\pi/2$ to $\alpha = \pi/2$ and show a clear excess of events at small $|\alpha|$ values. What we observe is consistent with the expectations of Sec. II where the region near $\alpha = \pi/2$ is predicted to be the only one not depleted by destructive interference (see also Fig. 28a in Sec. VI B 3). A representative comparison of the data and theory is obtained using the quantity (Monte Carlo)/DATA (Fig. 13). The α distribution shown in Fig. 12 for each Monte Carlo is divided bin by bin by the data distribution, also shown in Fig. 12. Again the Monte Carlos that do not take into account initial-final state interference (Fig. 13b,c) show a clear excess of events in the regions expected to be more depleted by color coherence. However, it should be noted that residual differences remain with the data, even in the case of HERWIG and PYTHIA+. For brevity, we will use the term "*interference patterns*" to refer to the shapes of the data distributions in Figs. 10, 11, and 12.

Since color coherence is approximated to different degrees in the four shower Monte Carlos considered, we can draw the following conclusions:

1. The variables R, η_3 and α discriminate between the Monte Carlos (see Figs. 10, 11, and 12).

2. The color coherence is responsible for the differences between the predictions. In fact, the agreement with the data improves as higher degrees of color coherence are implemented. Moreover, these variations are in accord with the description

of Sec. II. The η_3 distribution and, accordingly, the R distribution become wider. The α distribution shows the effect of the α-dependent suppression.

3. The *interference patterns* exhibit the color coherence in the data. The effect survives the non-perturbative phase of the hadronization as well as the smearing due to the underlying event.

This work is a first attempt to isolate color coherence effects in $p\overline{p}$ collisions. The agreement between data and Monte Carlo is not perfect and it is probably affected also by other mechanisms different from angular ordering. More understanding is necessary to give a quantitative estimate of the Monte Carlos' abilities to describe interference and radiation in general.

In Sec. VI we will present a collection of Monte Carlo studies that will improve the confidence in these results and allow to obtain further insight on the mechanisms of color coherence.

V. SYSTEMATIC UNCERTAINTIES

The sources of systematic uncertainties on the measurement of the η_3, R, and α distributions can only affect the shape of the spectra. Since all distributions are normalized to unit area, no contribution is expected from effects that can change only the overall rate of events, such as the error on the integrated luminosity. When comparing the data to the Monte Carlo, the major sources of systematic uncertainties are the calorimeter response, the structure functions, and the tuning of the fragmentation in the Monte Carlo.

The uncertainty in the calorimeter response to hadrons arises from several sources. For hadron momenta below 10 GeV/c, the response is determined using the *in situ* calibration by charged particles in $p\bar{p}$ data, whose dominant uncertainty is the subtraction of energy from accompanying π^0's. At higher pion momenta, systematic effects come from the uncertainty in the response across the face of the calorimeter and the response in cracks between calorimeter cells. These cracks are uninstrumented regions located at the boundaries between different parts of the calorimeter (cracks at $|\eta| = 2.5$ and $|\eta| = 0$) and at the boundaries between calorimeter modules in the ϕ coordinate (ϕ cracks).

First, we probe the effect of the detector on the *interference patterns.* Fig. 14 shows the α, R and η_3 distributions of HERWIG events simulated with the ideal calorimeter (*IDEAL SIM*), compared to those of the same events simulated with the CDF detector (*CDF SIM*). In order to facilitate the comparison with the size of the coherence effect shown in Figs. 10, 11, and 12, Fig. 14d shows the α distribution predicted by ISAJET + CDF SIM superimposed on the two HERWIG predictions. This latter plot uses the wider α-bins, which are chosen for the study of the small systematic errors that are presented below. Even in the case of the α distribution, which is the most sensitive of the three, the detector effect is smaller than the coherence effect. We conclude that the smallness of the detector effect indicates that the uncertainties in the systematics associated with the calorimeter response are negligible compared with the size of the observed coherence effect.

The effect of the detector on the *interference patterns* is small because the distributions are primarily related to jet angular coordinates, which are measured with a good resolution. The resolution on the jet energies has some influence through the event selection cuts on E_{T1} and E_{T3} and, more importantly, through the jet ordering by decreasing transverse energy. For instance, a large contribution to the effect of Fig.

14a comes from switching the order of the two leading jets. Such a misidentification of the second-E_T jet can occur because of fluctuations in the energy measurement.

The effects of the systematics on the η_3, R, and α distributions can be estimated with the Monte Carlo by varying the simulation parameters within their uncertainties. We report here on the studies on the α distribution. As expected, all the effects are negligible compared to the size of the coherence effect.

Fig. 15a shows that the HERWIG + CDF SIM α distribution does not change if the third jet E_T, for jets in the region $2 < |\eta_3| < 3$, is corrected to reproduce the observed η_3 distribution (see Fig. 10). Figs. 15b-c show the effects, on the α distribution, due to 100% variations of the other crack sizes. Figs. 15d-e show the impact of an error in the overall calibration of the detector response to single particles and of the uncertainty in the relative calibration between the scintillator and the gas calorimeter. Fig. 15f shows the effect of a 10% change in the relative calibration of the transition region $(0.7 < |\eta| < 1.3)$ covered by the End Wall hadronic calorimeter, as shown in Fig. 7.

Fig. 16 shows the influence of the theoretical uncertainties. Since in this case we do not need to compare the Monte Carlo with the real data, we use the ideal calorimeter simulation. The main theoretical uncertainties affecting the distribution under study are those on the fragmentation and on the parton distribution functions. The effect of the hadronization is investigated by switching off the non perturbative fragmentation stage at the end of the shower evolution in HERWIG (Fig. 16a). The uncertainty in the fragmentation was also studied by comparing different versions of the HERWIG fragmentation scheme (Fig. 16b). Finally Figs. 16c-e show the effect of the uncertainty in the parton distribution functions. The α distributions obtained with the parametrizations DO set 1 [23], EHLQ sets 1 and 2 [24], and MT set S1 [25] are compared. Again all the effects are negligible compared with the size of the coherence effect.

VI. COLOR COHERENCE IN THE SHOWER MONTE CARLOS

In order to obtain further insight on the mechanisms of color coherence, to improve the confidence in the results of the preceding sections and to understand the impact of different approximation schemes, we present here a collection of studies performed with HERWIG and PYTHIA.

Section VI A is devoted to showing that the ability of HERWIG to reproduce the *interference patterns* lies in the implementation of initial-final state coherence and cannot be ascribed to other dynamic properties. This is already evident for PYTHIA, since PYTHIA and PYTHIA+ differ only in the implementation of initial-final state coherence.

In Sec. VI B the sensitivity of the *interference patterns* to color flow is further investigated, by isolating, in the Monte Carlo, the few ingredients crucial to the explanation of the observed effects. It is further shown that the first gluon emission is very important in determining the third jet direction and that, in the gauge used by the Monte Carlo, initial state radiation dominates the production of the third jet.

These facts explain in more detail why PYTHIA does not reproduce the *interference patterns.* In this regard, as shown below, it is, in effect, equivalent to PYTHIA-off, where the angular ordering simulation is completely switched off. Section VI B also contains a more detailed description of the approximation in which PYTHIA+ implements initial-final state coherence and the effect on the absolute scale of the distributions for η_3, R, and α.

When we compare the simulated processes only amongst themselves, the events are not processed through the CDF detector simulation. We use, instead, the fast simulation of an ideal calorimeter, described in Sec. III, where the particle's energy is exactly measured.

A. The HERWIG incoherent and coherent subsamples

We first divide the HERWIG sample in two subsamples. The events in the first subsample are generated from LO processes where at least one color line flows from the initial to the final state. Hence, these processes contain the initial-final state coherence and are expected to be responsible for the formation of *interference patterns* in the Monte Carlo distributions. For brevity, we call them *coherent* events. In contrast, the initial and final states of the second sample are not color connected. These events do not contain initial-final state coherence and they will be called *incoherent* events. *Incoherent* events are not expected to contribute to the observed effect.

Fig. 17 shows the η_3, R, and α distributions for the HERWIG *coherent* and *incoherent* subsamples superimposed on ISAJET predictions. The distributions for the *incoherent* events have the same behaviour as the ISAJET distributions, whereas the distributions for the *coherent* subsample have shapes similar to those of the data (and of the HERWIG global sample). The *coherent* sample, then, is clearly responsible for the better agreement of HERWIG with the data.

This test is striking, but not definitive. In fact, the *coherent* and *incoherent* subsamples differ from each other not only for the color flow, but also for other dynamic properties that could, in principle, be relevant in determining the shape of the distributions of η_3, R, and α. As one can easily verify by considering the color flow in all the 2 → 2 Feynman diagrams, the *incoherent* sample includes exclusively LO processes involving only quarks or antiquarks in the external states. On the contrary, the *coherent* sample is comprised mostly of LO processes involving gluons. One might suspect that the differences in our distributions could be due to the different dynamics of these diverse processes.

We then perform a new test with a stronger discriminating power. Let us consider the two similar processes $q\overline{q'} \rightarrow q\overline{q'}$ (class A) and $qq' \rightarrow qq'$ (class B) shown in Fig. 18. Both classes A and B proceed through gluon exchange in the t-channel, as shown in Fig. 18c, but they differ in the color flow: classes A and B belong to the *incoherent* and *coherent* subsamples, respectively. Hence, the main and essentially the only difference between the two classes of processes resides now in the color flow. For this reason, a comparison between the predicted distributions of any variable for the two classes would help to establish whether that variable is sensitive to initial-final state color interference.

A complementary test would be to plot the same variable for processes that, dynamically, are totally different from each other, having in common only the pattern of color flow from the initial to the final state. For this test we choose, from the *coherent* subsample, the three processes illustrated in Fig. 19: $gg \rightarrow gg$ (class G) $q\overline{q} \rightarrow q'\overline{q'}$ annihilations (class S) and $qq' \rightarrow qq'$ (class B). If the distributions for the α variable for these three classes are similar, this would imply that color flow is the dominant dynamic property governing the behaviour of α.

Fig. 20a shows the α distributions for the classes A and B . The two distributions are clearly unlike, confirming that the effect of initial-final state color coherence in HERWIG is indeed the effect exhibited by the *interference patterns.*

Fig. 20b shows the α distributions for the classes B, S and G. The α distributions are very similar for the three classes. This result shows that α is more sensitive to color flow than to other dynamic properties such as the type of partons involved in the hard scattering, or the channel through which the hard scattering proceeds.

B. Angular ordering in PYTHIA

We now present a thorough discussion of the differences between PYTHIA and PYTHIA+, which will serve to highlight the key ingredients required to generate the observed *interference patterns.*

In PYTHIA, the angular ordering is not effective on the first gluon emission. The shower evolution is performed in the rest frame of the hard scattering where the final state parton pair subtends an opening angle of 180°. A color antenna spanned between the two final partons or between the two initial partons thus constrains the maximum angle for the emission to be 180°: the net result is no restriction. In $p\overline{p}$ collisions, however, a color dipole may span the initial and the final state (initial-final state antenna). It is here that the scattering angle of the color flow constrains the maximum opening angle of an emission cone. PYTHIA does not implement angular restrictions on the emission from such an antenna.

We will show that the first emission has a dominant influence on the third-E_T jet direction and that, in the Monte Carlo, the third jets are mainly produced by initial state radiation. Hence, the crucial ingredient for the emergence of the *interference patterns* in the Monte Carlo is the implementation of the angular restriction on the emission of the first gluon by the initial state prong of the initial-final state antennas. This point is, in fact, confirmed by the comparison between the distributions predicted by PYTHIA and PYTHIA+. As described in detail in the Sec. VI B 3 below, PYTHIA+ implements the angular restriction for the first emission of the initial-final state antennas. Since this is the only difference with PYTHIA, it must be the reason for the discrepancy in the predicted distributions.

1. Angular ordering for the first emission

In order to show the influence of the the first emission on the third jet direction, we use a feature of PYTHIA that allows us to constrain, in a fixed cone, the first gluon emission of time-like showers. We then use restriction cones of fixed size, instead of the QCD prescription, to study the behaviour arising from the restriction cone size. *Coherent* events are generated by the process $qq' \rightarrow qq'$, confining the first emissions within cones of apertures $\delta = 1$ *rad* and $\delta = 0.5$ *rad* respectively.

Fig. 21 compares the distributions of the three variables η_3, R and α for the two fixed restriction cones with those obtained for no restriction (180°) . The effect of applying the angular restriction has the expected trend: the η_3 and R distributions become wider and the α distribution becomes lower in the central region. The effect is unequivocal for $\delta = 0.5$ rad and it is very small for $\delta = 1$ *rad*.

Actually, the case $\delta = 1$ *rad* should be representative of the average angular restriction imposed by color coherence that is expected in this analysis. Since the second jet is constrained in the central calorimeter, $|\eta_2| < 0.7$, all the QCD restriction cones extending to the beam line (region B in Fig. 4) have an aperture greater than 0.9 *rad*. However, the effect for $\delta = 1$ rad is much smaller than the one observed in the data because, for this PYTHIA case, the angular restriction on the first emissions from the initial state is not implemented (see Sec. VI B 2 below).

In summary, the first emission is important for defining the third jet direction (Fig. 21b), but the angular restriction in the final state alone cannot reproduce the right size of the effect (Fig. 21a).

2. Angular ordering for the initial state radiation

Radiation in the initial state is indeed important as it provides a major contribution to the third jet production. To show this we need to separate, in the Monte Carlo samples, the third jets radiated from the initial state from those radiated from the final state. We use the HERWIG Monte Carlo for this study.

For this purpose we examine the fraction, f_3, of the third jet energy radiated by the final state. In principle, gauge invariance prevents us from associating the emission to a specific parton branch: it is the color antenna that radiates. However, in a Monte Carlo, a specific gauge choice is made and we can identify the parton from which a gluon is radiated. Then, for each particle generated by the Monte Carlo, we can determine whether its energy derives from the initial state, the final state, or from both states.

We calculate the third jet energy radiated from the final state by summing the energy of those particles that are product of final state radiation and belong to the third jet (namely those falling inside the clustering cone). The fraction f_3 is, then, this energy sum divided by the third jet energy (calculated as the sum over all the particles belonging to the jet). We divide the whole sample in two categories: the subset *init*, containing events with a third jet produced mainly by initial state radiation ($f_3 < 0.2$) and the subset *fin*, containing events with a third jet that has at least 20% of its energy coming from final state radiation ($f_3 > 0.2$). Table 3 shows the relative frequencies of these categories for the Monte Carlo HERWIG. Most of the third jets receive a substantial contribution from the initial state radiation.

We also look at the content of *incoherent* and *coherent* events in the two *init* and *fin* samples. Table 4 shows that in both samples the *coherent* events are the majority. Fig. 22 shows that the coherence effect manifests itself in both the *init* and the *fin* samples, as a difference between the *incoherent* and *coherent* distributions. The *fin* sample distribution is unusual because it gets contribution from third jets produced by the radiation from the final state parton that generated the first jet in the event. These third jets, because of the collinear singularities, are clustered around the first jet, that is located near $|\Delta\phi| = \pi$ and $H = 0$ in Fig. 5, corresponding to $\alpha = 0$.

In conclusion, the coherence effect is present in the radiation from the final state as well as from the initial state, but the fraction of events with a significant contribution to the third jet energy that arises from final state radiation is too small to produce a visible effect by itself. In order to reproduce the size and shape of the effect observed in the data, the angular ordering must be implemented also for the initial state radiation.

3. Comparison of implementations of coherence in PYTHIA

Here, we examine briefly the new implementations of angular ordering in PYTHIA+. Let us consider the four partons involved in a 2 → 2 scattering. For each parton associated with an initial-final state antenna, PYTHIA+ restricts the first emission according to the QCD prescription. In this context, "first" emission means the branching closest to the hard scattering, as shown in Fig. 23.

If the emitting parton is a gluon, it contributes to two different color dipoles. Fig. 24 illustrates this case. Only one of the two dipoles is an initial-final state antenna. The other dipole lies entirely in either the initial or the final state and, consequently, does not require an effective restriction, because it has an opening angle of 180°. In the approximation scheme of PYTHIA+, the choice of which dipole radiates first is made randomly with equal probability.

The implementation of the phase space restriction described above is the only distinction between PYTHIA and PYTHIA+. However, it makes the difference in Figs. 10, 11, and 12. On the other hand, the coherence implemented in PYTHIA does not show any effect in the *interference patterns.* Fig. 25 summarizes all these results comparing the Monte Carlo samples between themselves. The ideal calorimeter simulation is used in order to obtain a comparison independent of the CDF detector details. Fig. 25a show the PYTHIA distributions superimposed on those of the sample PYTHIA-off, which is generated with unconstrained radiation. No significant difference appears for any of the distributions. Fig. 25 compares also the PYTHIA (b) and PYTHIA+ (c) distributions with the HERWIG predictions. PYTHIA+ has a behaviour similar to HERWIG, while PYTHIA is different.

The change in the η_3 distribution from PYTHIA to PYTHIA+, also suggests that the transverse energy of the third jet E_{T3} is sensitive to color coherence. Fig. 26 shows the E_{T3} distributions of PYTHIA (a) and PYTHIA+ (b) compared to the HERWIG prediction (1) and to the data (2). In this last case the PYTHIA events are simulated through the CDF detector. The E_{T3} spectrum of PYTHIA+ is in better agreement with HERWIG and the data.

As an additional test of the inadequacy of the PYTHIA implementation, Fig. 27 shows the α distributions for the classes A (*incoherent*) and B (*coherent*) defined in Sec. VI A. Unlike the situation for HERWIG (Fig. 20a) and PYTHIA+ (Fig. 27b), there is no significant difference between the *coherent* and the *incoherent* distributions for PYTHIA (Fig. 27a).

Up to this point, in order to facilitate the comparisons between the various probability distributions, all the distributions have been normalized to unit area. In order to understand the absolute effect of the angular restrictions on the characteristics of the third-Et jets, it is also interesting to compare distributions normalized to the same integrated luminosity. Fig. 28 shows the comparison, on an absolute scale, between the samples of PYTHIA+ and PYTHIA-off. This figure clearly illustrates that the *interference patterns* are generated by depletion in given regions of the distributions. The depletion is, of course, a direct consequence of the radiation suppression outside the restriction cones. The total probability for generating a third jet becomes smaller because of the color coherence.

VII. CONCLUSIONS

We have presented in this paper direct evidence for color coherence phenomena in $p\bar{p}$ collisions. The result has been obtained by studying kinematical correlations between the second- and the third- most energetic jets in multijet events. We have compared our data with several shower Monte Carlo calculations that implement, with differing levels of accuracy, the quantum coherence in the gluon radiation process. The comparison of the shape of third jet distributions has allowed us to single out the interference between initial and final state gluon emission from color connected partons as the origin of the observed correlations. We have verified that HERWIG and a modified version of the PYTHIA Monte Carlo (now implemented in version 5.7) reproduce the data better than ISAJET and PYTHIA version 5.6. This confirms complementary findings from e^+e^-physics supporting the theoretical result that color coherence phenomena can be included in a shower Monte Carlo despite their quantum nature. It is expected that future quantitative studies, extending this analysis for example to different jet energy ranges or to different event samples, will provide additional tests of QCD color coherence and will result in further improvements in the theoretical models. Investigations should focus on the residual disagreements remaining between the data and the predictions of the Monte Carlos implementing color coherence. As soon as the relevant calculations are available, it will also be interesting to compare the distributions studied in this work with parton level calculations [26] based on next-to-leading order QCD matrix elements [27]. Since the first emission is particularly important to determine the third jet direction, as shown in Sec. VI B 1, we expect this calculation to be able to describe our measurements.

ACKNOWLEDGMENTS

We are deeply thankful to T. Sjöstrand for his constant and active interest in this work. His contribution was fundamental for our complete understanding and interpretation of the results. We thank the Fermilab Accelerator Division, the Computer Division, and the CDF technical staff for their dedicated effort that made this experiment possible. This work was supported by the Department of Energy, the National Science Foundation, the Natural Sciences and Engineering Research Council of Canada, the Italian Istituto Nazionale di Fisica Nucleare, the Ministry of Science, Culture and Education of Japan, and the A.P. Sloan Foundation.

References

[1] JADE Collaboration, W. Bartel et al., Phys. Lett. B **101**, 129 (1981); Z. Phys. C **21**, 37 (1983);
TPC/2γ Collaboration, H. Aihara et al., Phys. Rev Lett. **54**, 270 (1985); Z. Phys. C **28**, 31 (1985); Phys. Rev Lett. **57**, 945 (1986);
TASSO Collaboration, M. Althoff et al., Z. Phys. C **29**, 29 (1985);
MARK2 Collaboration, P.D. Sheldon et al., Phys. Rev Lett. **57**, 1398 (1986).

[2] OPAL Collaboration, M.Z. Akrawy et al., Phys. Lett. B **247**, 617 (1990);
OPAL Collaboration, M.Z. Akrawy et al., Phys. Lett. B **261**, 334 (1991);
OPAL Collaboration, P.D. Acton et al., Phys. Lett. B **287**, 401 (1992);
OPAL Collaboration, P.D. Acton et al., Z. Phys. C **58**, 207 (1993).

[3] For reviews, and ref.'s to the original literature see: Yu.L. Dokshitzer, V.A. Khoze and S.I. Troyan, in *Perturbative QCD*, ed. A.H. Mueller, Singapore: World Scientific (1989), 241;
Yu.I. Dokshitzer, V.A. Khoze, S.I. Troyan and A.H. Mueller, *Rev. Mod. Phys.* **60** (1988), 373.

[4] S. Bethke and J.E. Pilcher, Ann. Rev. Nucl. Part. Sci., vol. **42** (1992) 251;
T. Hebbeker, *Phys. Rep.* **217** (1992), 69.

[5] J.E. Huth and M.L. Mangano, Ann. Rev. Nucl. Part. Sci., vol. **43** (1993) 585.

[6] For a review, see: A. Bassetto, M. Ciafaloni and G. Marchesini, *Phys. Rep.* **100** (1983), 201.

[7] M. Dell'Orso, CDF Collaboration, Proceedings of the 8th Topical Workshop on

Proton-Antiproton Collider Physics, 1-5 Sept. 1989, Castiglione della Pescaia (Italy), eds. G. Bellettini and A. Scribano, World Scientific Publ., 177;
R. M. Harris, CDF Collaboration, Proceedings XXVIIth Rencontres de Moriond, 22-28 March 1992, Les Arcs, Savoie (France) eds. J. Tran Thanh Van, Editions Frontieres, 3;
E. Meschi, CDF Collaboration, Proceedings of the DPF Meet. Am. Phys. Soc., 10-14 Nov 1992, Batavia (Illinois), eds. C.H. Albright et al., World Scientific Publ., 1117.

[8] F. Borcherding, D0 Collaboration, Fermilab Report No. FERMILAB-Conf-93/388-E, 1991 (to be published in the Proceedings of the 9th Topical Workshop on Proton-Antiproton Collider Physics, 18-22 Oct. 1993, Tsukuba, Japan).

[9] H.-U. Bengtsson, *Comp. Phys. Comm.* **31** (1984), 323.

[10] G. Marchesini and B. Webber, Nucl. Phys. B **310**, 461 (1988).

[11] H.-U Bengtsson and T. Sjöstrand, *Comp. Phys. Comm.* **46** (1987), 43;
T. Sjöstrand and M. Bengtsson, *Comp. Phys. Comm.* **43** (1987), 367;
T. Sjöstrand, CERN-TH 6488 (1992).

[12] F. E. Paige and S. D. Protopopescu, BNL Report No. 38034 (1986).

[13] M. Ciafaloni, Nucl. Phys. B **296**, 249 (1987); S. Catani, F. Fiorani, G. Marchesini, Phys. Lett. **234**, 339 (1990);

[14] R.K. Ellis, G. Marchesini and B. Webber, *Nucl. Phys.* **B286** (1987), 643.

[15] J. Huth *et al.*, Proceed. of the Summer Study on High Energy Physics (1990), Snowmass, Colorado, 134.

[16] F. Abe *et al.*, Phys. Rev. D **45**, 1448 (1992).

[17] F. Abe *et al.* Nucl. Instr. Meth. A **271**, 387 (1988).

[18] F. Abe *et al.*, Phys. Rev. Lett. **65**, 2243 (1990).

[19] F. Abe *et al.*, Phys. Rev. D **45**, 1448 (1992).

[20] F. Abe *et al.*, Phys. Rev. Lett. **69**, 2896 (1992).

[21] F. Abe *et al.*, Phys. Rev. Lett. **62**, 613 (1989).

[22] T. Sjöstrand, private communication.

[23] D. Duke and J. Owens, Phys. Rev. D **30**, 49 (1984).

[24] E. Eichten *et al.*, Rev. Mod. Phys. **56**, 579 (1984).

[25] W. Tung and J.G. Morfin, Z. Phys. C **52**, 13 (1991).

[26] S.Ellis, Z.Kunszt and D. Soper, *Phys. Rev. Lett.* **64** (1990), 2121; F.Aversa, P.Chiappetta, M. Greco and J.P. Guillet, *Z. Phys.* **C46** (1990), 253.

[27] R.K. Ellis and J.C. Sexton, *Nucl. Phys.* **B269** (1986), 445.

System	η range	Energy resolution	Thickness
CEM	$\|\eta\| < 1.1$	$13.7\%\sqrt{E_T} \oplus 2\%$	$18X_0$
PEM	$1.1 < \|\eta\| < 2.4$	$28\%\sqrt{E} \oplus 2\%$	$18X_0 - 21X_0$
FEM	$2.4 < \|\eta\| < 4.2$	$25\%\sqrt{E} \oplus 2\%$	$25X_0$
CHA	$\|\eta\| < 0.9$	$50\%\sqrt{E_T} \oplus 3\%$	$4.5\lambda_0$
WHA	$0.7 < \|\eta\| < 1.3$	$75\%\sqrt{E} \oplus 4\%$	$4.5\lambda_0$
PHA	$1.3 < \|\eta\| < 2.4$	$90\%\sqrt{E} \oplus 4\%$	$5.7\lambda_0$
FHA	$2.4 < \|\eta\| < 4.2$	$130\%\sqrt{E} \oplus 4\%$	$7.7\lambda_0$

Table 1: Summary of CDF calorimeter properties. The symbol $\oplus$ signifies that the constant term is added in quadrature in the resolution. Thicknesses are given in radiation lengths for electromagnetic calorimeters and absorption lengths for hadronic calorimeters. The electromagnetic resolutions are for electrons and photons; the hadronic resolutions are for isolated pions.

	Data	HERWIG	ISAJET	PYTHIA-off	PYTHIA+	PYTHIA
Luminosity (pb^{-1})	4.2	5.5	5.9	5.8	5.8	5.8
After cuts 1,2,3,4	13983	15706	16145	15143	14540	16181
After cut 5	10649	11004	12261	10565	9085	11988
After cut 6	8201	8474	9444	8382	6940	9411

Table 2: The number of events in the data and the simulated samples. Each simulated sample originally contained 280000 events. See text for definition of the cuts.

sample	fraction of the total
init ($f_3 < 0.20$)	75%
fin ($f_3 > 0.20$)	25%

Table 3: Fraction of HERWIG events where the third jet is generated by initial state radiation (*init*) or final state radiation (*fin*).

sample	*coherent*	*incoherent*
init ($f_3 < 0.20$)	93%	7%
fin ($f_3 > 0.20$)	87%	13%

Table 4: *Incoherent* and *coherent* fractions in samples *init* and *fin*.

Figure Captions.

Fig. 1: Sketch of a $e^+e^- \to 3 - jet$ event. a) Partons exiting from the primary vertex. Soft radiation, represented by shadowing, is suppressed in the region between the two quarks relative to the other regions. b) Color flow for the same event. The color lines can be identified as directional antennas.

Fig. 2: Angular ordering. a) Feynman diagram of a final state shower. b) Color flow in the shower. c) Partons exiting from the primary vertex. The emitted radiation is constrained around the emitting parton, within a cone defined by the color-connected partner. A similar cone (not shown) confines radiation emitted by the partner.

Fig. 3: Phase space constraints for the first gluon emission in a $q\overline{q}$ annihilation. a) Feynman diagram of the hard scattering. b) Color lines flow from the initial to the final state, q and q' are color partners. c) Restriction cones for q and q'. Similar cones can be drawn for $\overline{q}$ and $\overline{q}'$.

Fig. 4: Spatial distribution of radiation for the 2 → 2 scattering of Fig. 3. a) Radiation from the emitting antenna is maximum in the overlap region C. Soft emissions from the antenna are forbidden outside the restriction cones A and B. b) Cross section of picture a).

Fig. 5: The observed spatial distribution of the third jet around the second jet. Each point represents the position of a third-E_T jet. The second jet axis corresponds to the origin. The circular region around the second jet is forbidden to other jets by

the clustering algorithm. The limit $|\Delta H| < 4$ is due to the calorimeter acceptance.

Fig. 6: The restriction cones of Fig. 4 as seen in the (α, R) space. The upper curved boundary corresponds to the limit $|\Delta\phi| < \pi$. The clustering algorithm prevents the jet axes from falling in the rectangular region $R < 0.7$. The boundaries between regions A, B, and C correspond to the case $\theta_s = 85°$.

Fig. 7: A side-view cross section of the CDF detector. The detector is forward-backward symmetric about the interaction region, which is in the center of the figure right side.

Fig. 8: Observed E_{T1} distribution compared to the predictions of: (a) HERWIG; (b) ISAJET; (c) PYTHIA; (d) PYTHIA+.

Fig. 9: Observed E_{T2} distribution compared to the predictions of: (a) HERWIG; (b) ISAJET; (c) PYTHIA; (d) PYTHIA+.

Fig. 10: Observed η_3 distribution compared to the predictions of: (a) HERWIG; (b) ISAJET; (c) PYTHIA; (d) PYTHIA+.

Fig. 11: Observed R distribution compared to the predictions of: (a) HERWIG; (b) ISAJET; (c) PYTHIA; (d) PYTHIA+.

Fig. 12: Observed α distribution compared to the predictions of: (a) HERWIG; (b) ISAJET; (c) PYTHIA; (d) PYTHIA+.

Fig. 13: Bin by bin ratio (Monte Carlo/DATA) of the (a) HERWIG, (b) ISAJET, (c) PYTHIA, (d) PYTHIA+ α distributions of Fig.12 over the data α distribution

also shwon in the same figure.

Fig. 14: α (a), R (b), and η_3 (c) distributions of HERWIG events simulated with the ideal calorimeter (*IDEAL SIM*), compared to those of the same events simulated with the CDF detector (*CDF SIM*). The comparisons show the effect of the detector on the *interference patterns.* The α distribution predicted by ISAJET + CDF SIM is also shown (d) superimposed on the HERWIG predictions: the effect of the detector (difference between *IDEAL SIM* and *CDF SIM*) is smaller than that of the color interference (difference between ISAJET and HERWIG).

Fig. 15: Effects on the HERWIG + CDF SIM α distribution, due to uncertainties in the calorimeter response: (a-c) 100% variations of the η and ϕ crack sizes; (d) one sigma variation in the overall calibration of the detector response to single particles; (e) 10% variation in the relative calibration between the scintillator and the gas calorimeters. (f) 10% variation of the jet energy scale in the End Wall region $0.7 < |\eta| < 1.3$

Fig. 16: Effects on the HERWIG + IDEAL SIM α distribution, due to theoretical uncertainties: (a) hadronization; (b) fragmentation scheme; (c-e) parton distribution functions.

Fig. 17: η_3 (a), R (b) and α (c) distributions for the HERWIG *coherent* (1) and *incoherent* (2) subsamples superimposed on the ISAJET distributions.

Fig. 18: (a) color flow in a class A process; (b) color flow in a class B process; (c) both classes A and B proceed through the t-channel gluon exchange.

Fig. 19: (a) example of class G process (gluon gluon scattering in any channel); (b) class S process ($q\bar{q}$ annihilation in the s-channel); (c) class B process (qq' scattering in the t-channel).

Fig. 20: HERWIG α distributions: (a) the A (*incoherent*) and B (*coherent*) classes; (b) the B, S, G classes (all *coherent*).

Fig. 21: PYTHIA: α, η_3, and R distributions for samples for which the angular restriction into a fixed cone is applied to the first emission in the final state: 1) cone size $\delta = 1$ rad (a); 2) cone size $\delta = 0.5$ rad (b). The distributions are superimposed on distributions for the sample generated with no angular restriction ($\delta = \pi$).

Fig. 22: HERWIG: α distribution of *coherent* events superimposed on that of *incoherent* events for the two samples *init* (a) and *fin* (b).

Fig. 23: The "first" emission is the branching closest to the hard scattering

Fig. 24: A gluon contributes to two different color dipoles. Only one of the two dipoles is an initial-final state antenna. The other dipole lies entirely in either the initial or the final state

Fig. 25: Comparisons between different Monte Carlo samples (*IDEAL SIM*) for the variables η_3 (1), R (2), and α (3): (a) PYTHIA compared to PYTHIA-off; (b) PYTHIA compared to HERWIG; (c) PYTHIA+ compared to HERWIG.

Fig. 26: E_{T3} distribution of PYTHIA (a) and PYTHIA+ (b) compared to: (1) the predictions of HERWIG (2) the data. The PYTHIA events compared to the data

are simulated through the CDF detector.

Fig. 27: α distribution for the class A (*incoherent*) compared to that for the class B (*coherent*): (a) PYTHIA; (b) PYTHIA+.

Fig. 28: PYTHIA-off compared to PYTHIA+ on an absolute scale: (a) α distribution; (b) R distribution; (c) η_3 distribution.

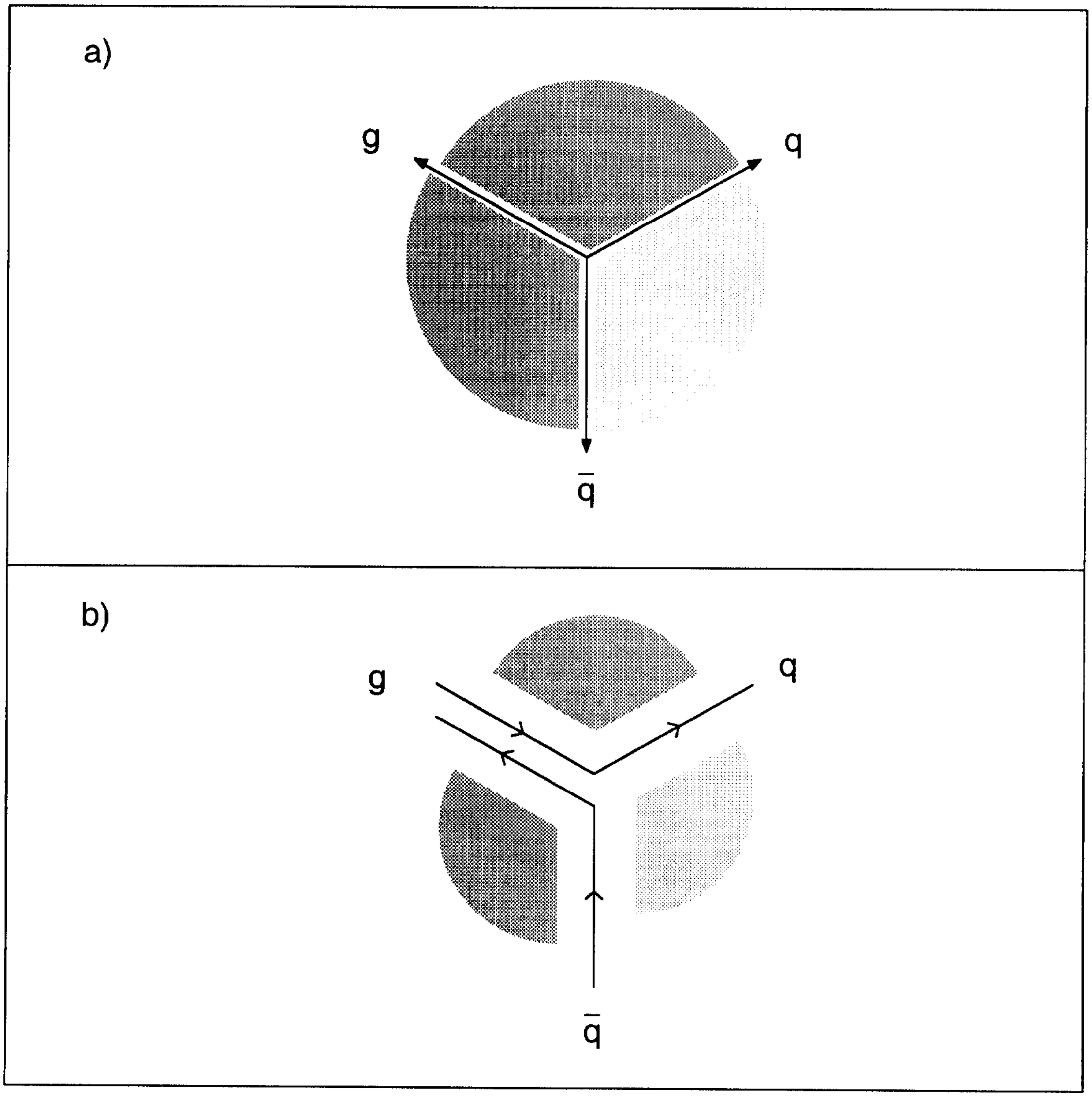

Figure 1:

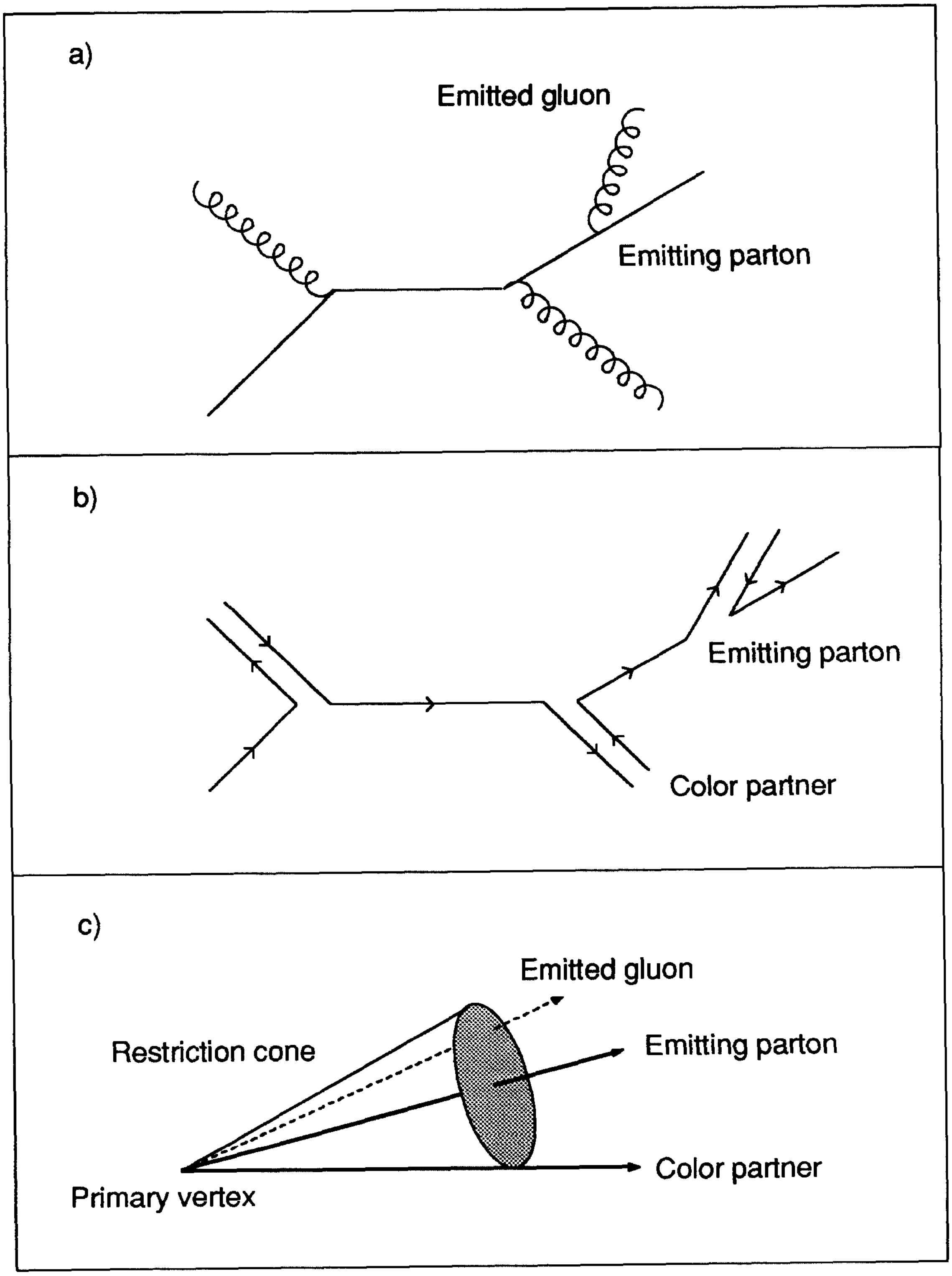
a)
Emitted gluon
Emitting parton
b)
Emitting parton
Color partner
c)
Emitted gluon
Restriction cone
Emitting parton
Color partner
Primary vertex

Figure 2:

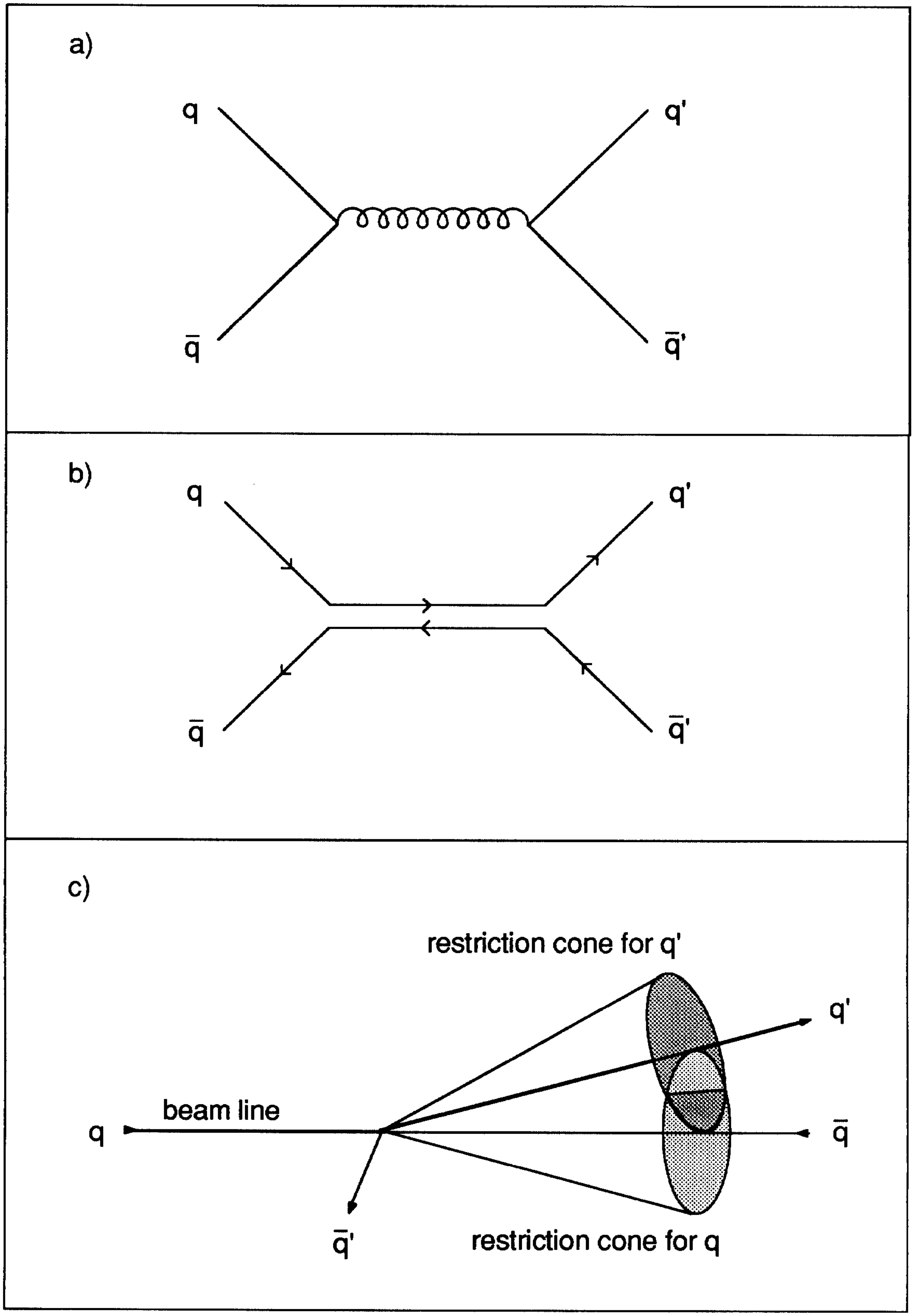
a)
q
q'
$\bar{q}$
$\bar{q}'$
b)
q
q'
$\bar{q}$
$\bar{q}'$
c)
restriction cone for q'
q'
beam line
q
$\bar{q}$
$\bar{q}'$
restriction cone for q

Figure 3:

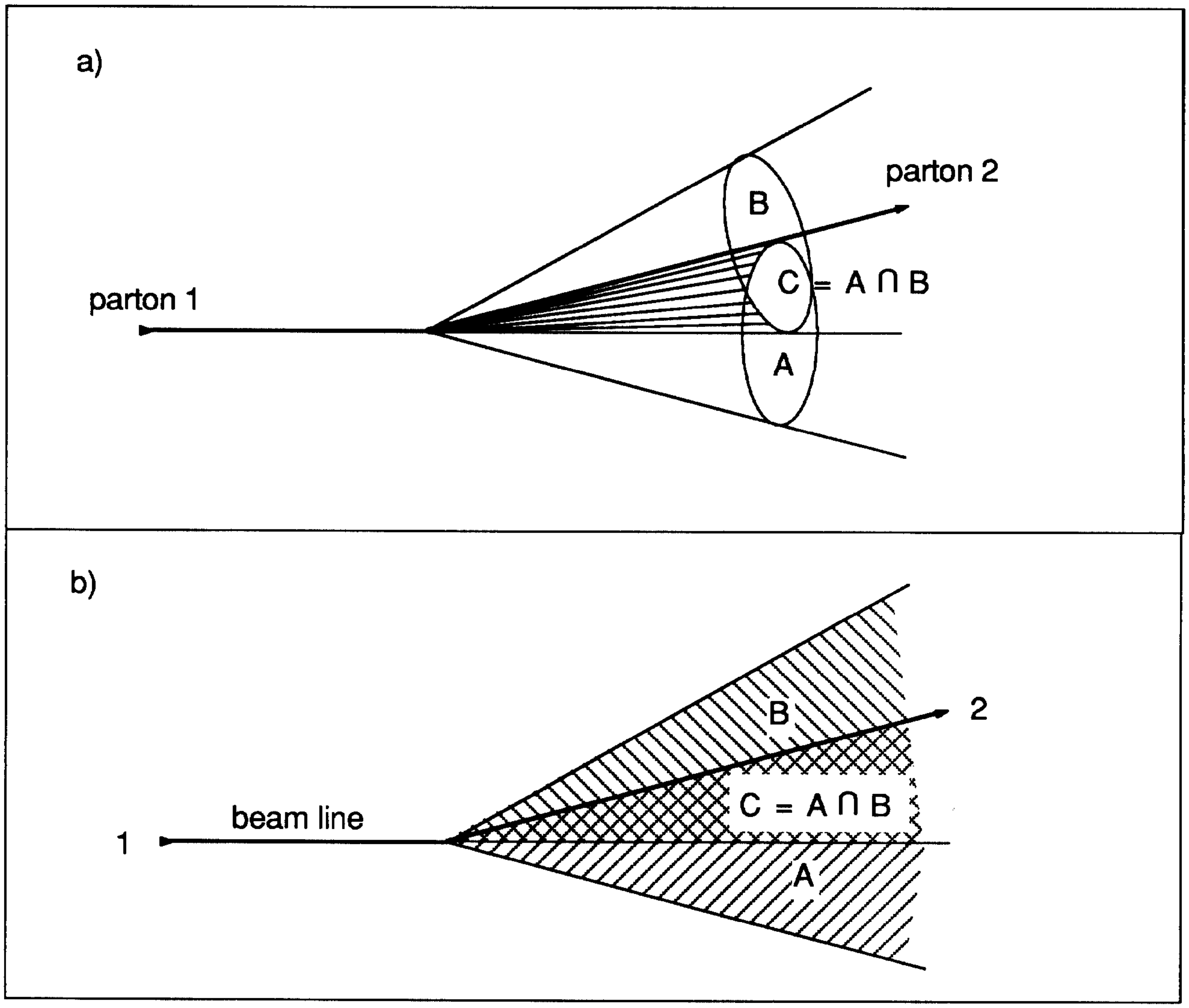

Figure 4:

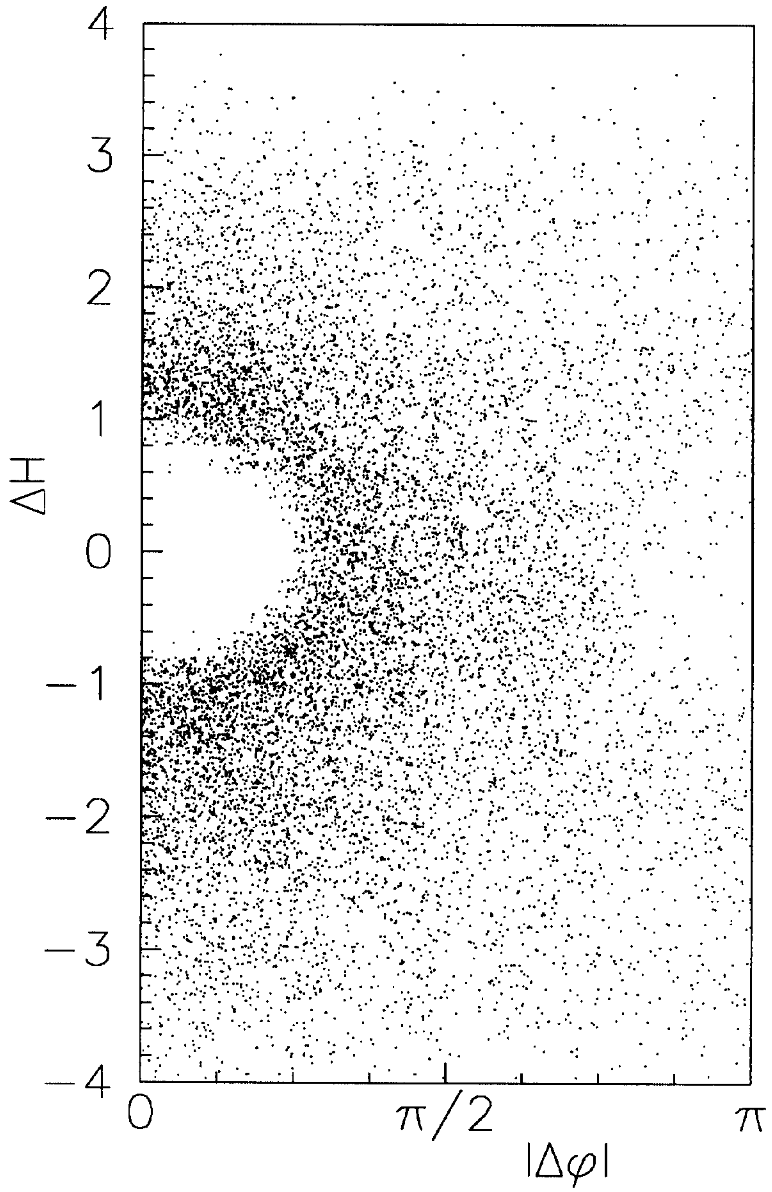

Figure 5:

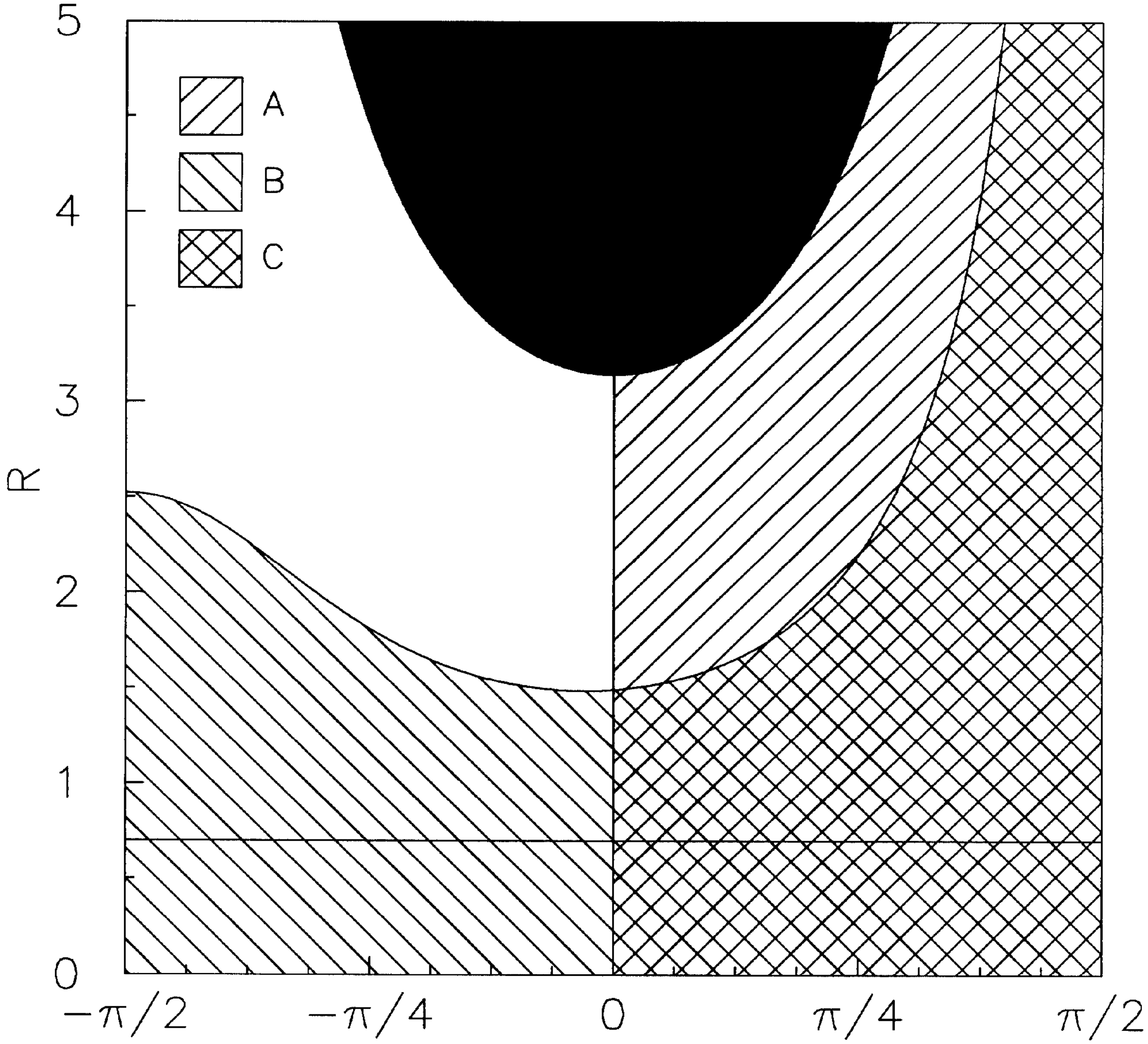

Figure 6:

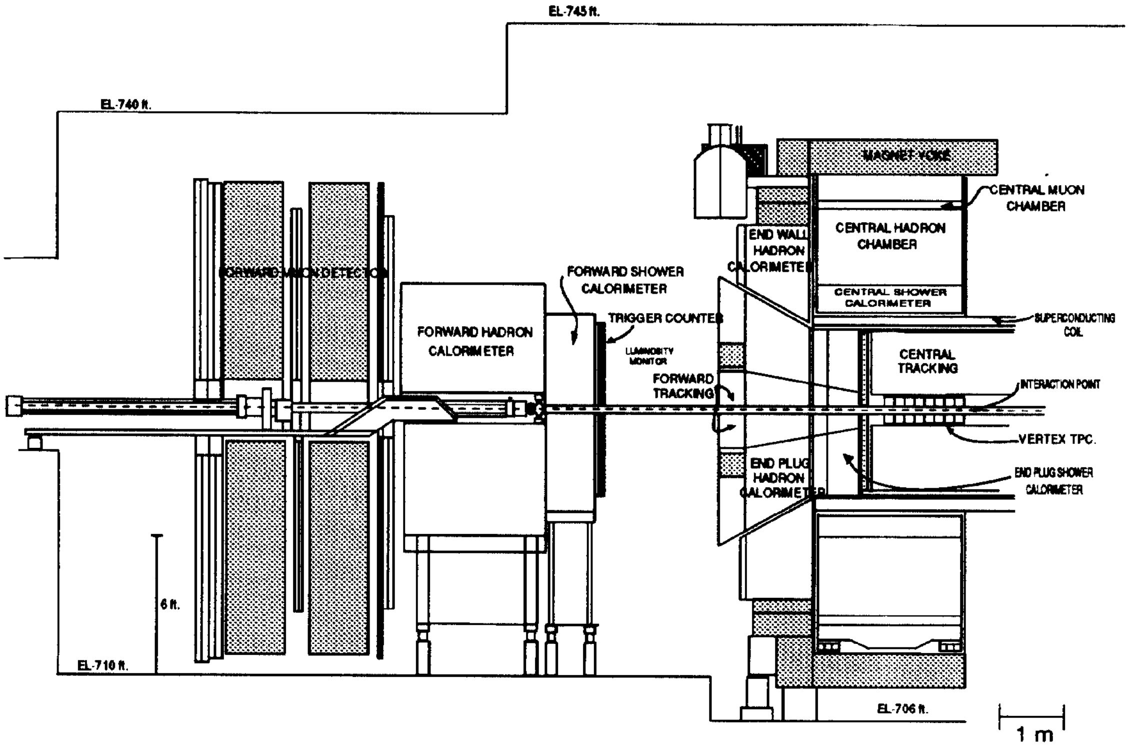
EL-745 ft.
EL-740 ft.
MAGNET YOKE
CENTRAL MUON CHAMBER
END WALL HADRON CALORIMETER
CENTRAL HADRON CHAMBER
FORWARD MUON DETECTOR
FORWARD SHOWER CALORIMETER
CENTRAL SHOWER CALORIMETER
SUPERCONDUCTING COIL
FORWARD HADRON CALORIMETER
TRIGGER COUNTER
LUMINOSITY MONITOR
CENTRAL TRACKING
FORWARD TRACKING
INTERACTION POINT
VERTEX TPC.
END PLUG HADRON CALORIMETER
END PLUG SHOWER CALORIMETER
6 ft.
EL-710 ft.
EL-706 ft.
1 m

Figure 7:

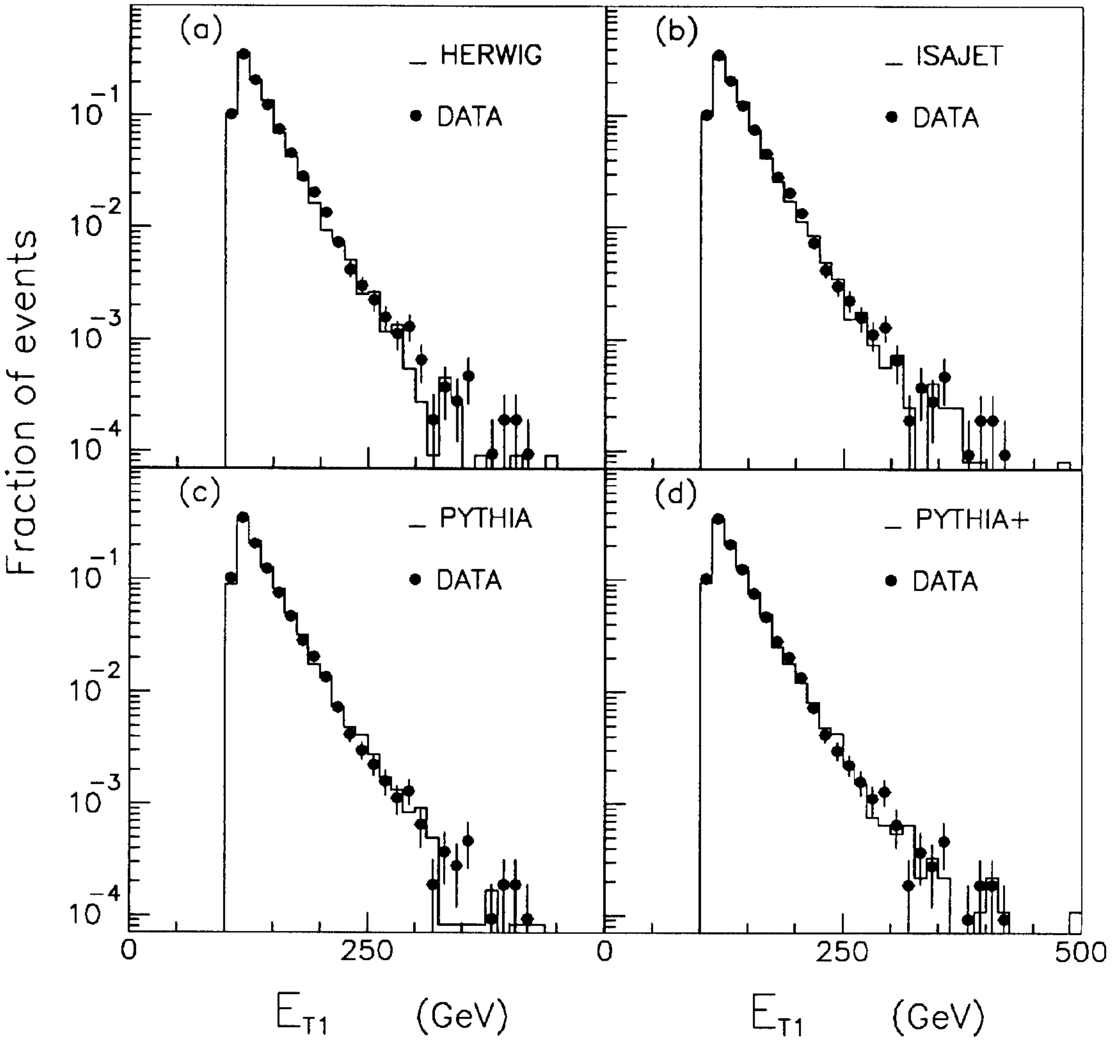
(a)
HERWIG
DATA
(b)
ISAJET
DATA
(c)
PYTHIA
DATA
(d)
PYTHIA+
DATA
Fraction of events
10^{-1}
10^{-2}
10^{-3}
10^{-4}
0
250
0
250
500
E_{T1} (GeV)
E_{T1} (GeV)

Figure 8:

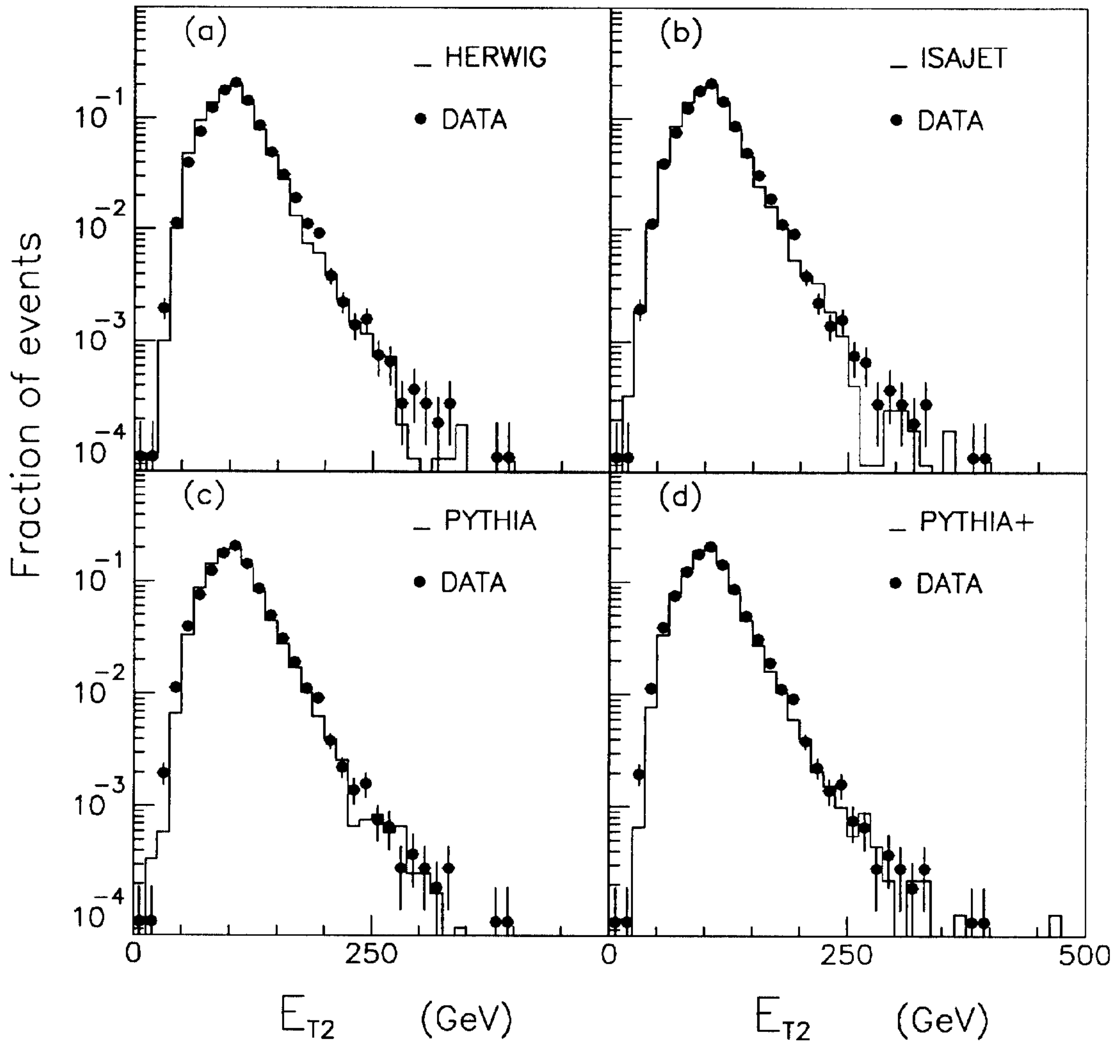
(a)
_ HERWIG
● DATA
(b)
_ ISAJET
● DATA
(c)
_ PYTHIA
● DATA
(d)
_ PYTHIA+
● DATA
Fraction of events
10^{-1}
10^{-2}
10^{-3}
10^{-4}
0
250
0
250
500
E_{T2} (GeV)
E_{T2} (GeV)

Figure 9:

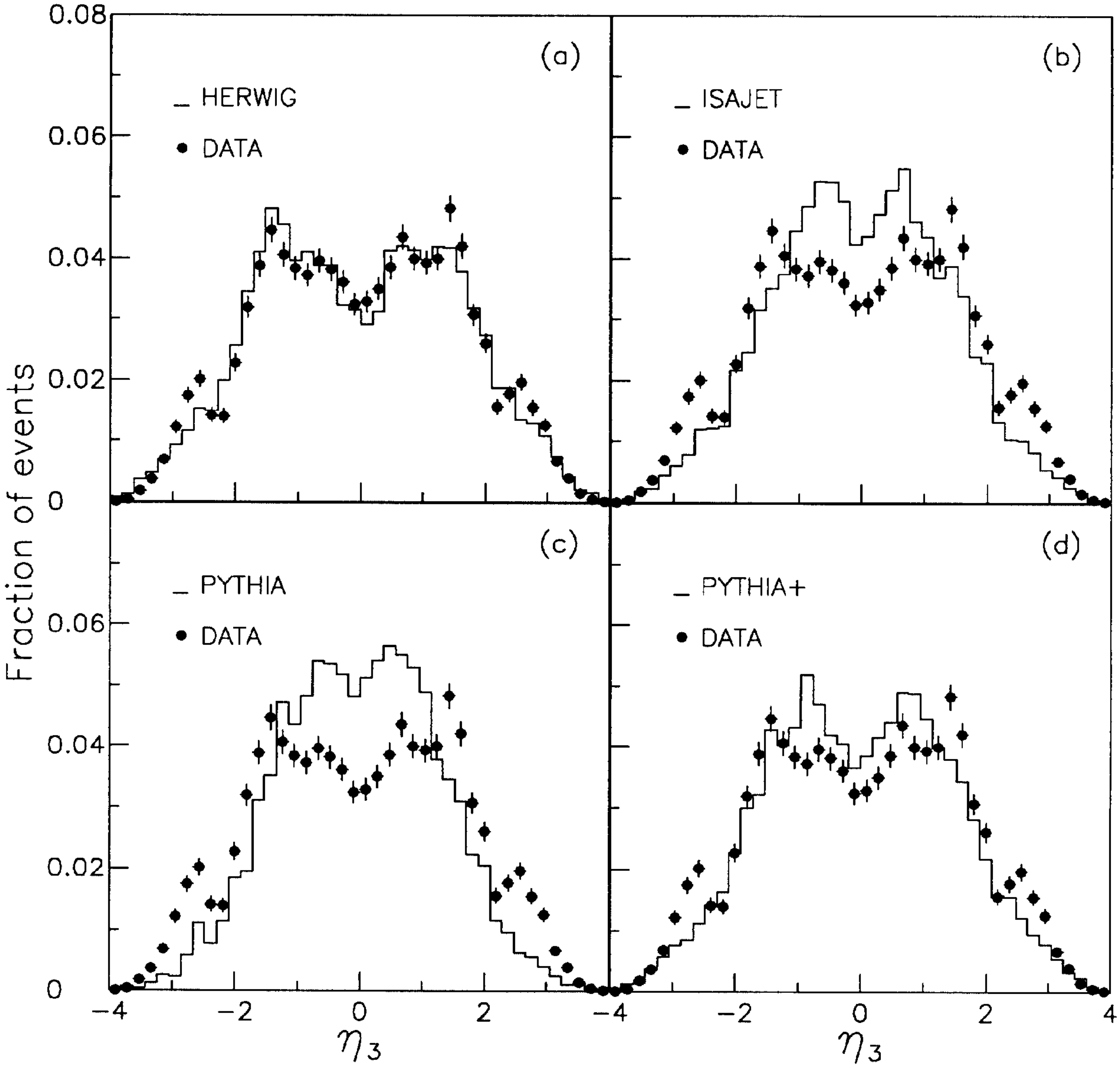

(a)
_ HERWIG
● DATA
(b)
_ ISAJET
● DATA
(c)
_ PYTHIA
● DATA
(d)
_ PYTHIA+
● DATA
Fraction of events
0.08
0.06
0.04
0.02
0
0.06
0.04
0.02
0
−4
−2
0
2
−4
−2
0
2
4
η_3
η_3

Figure 10:

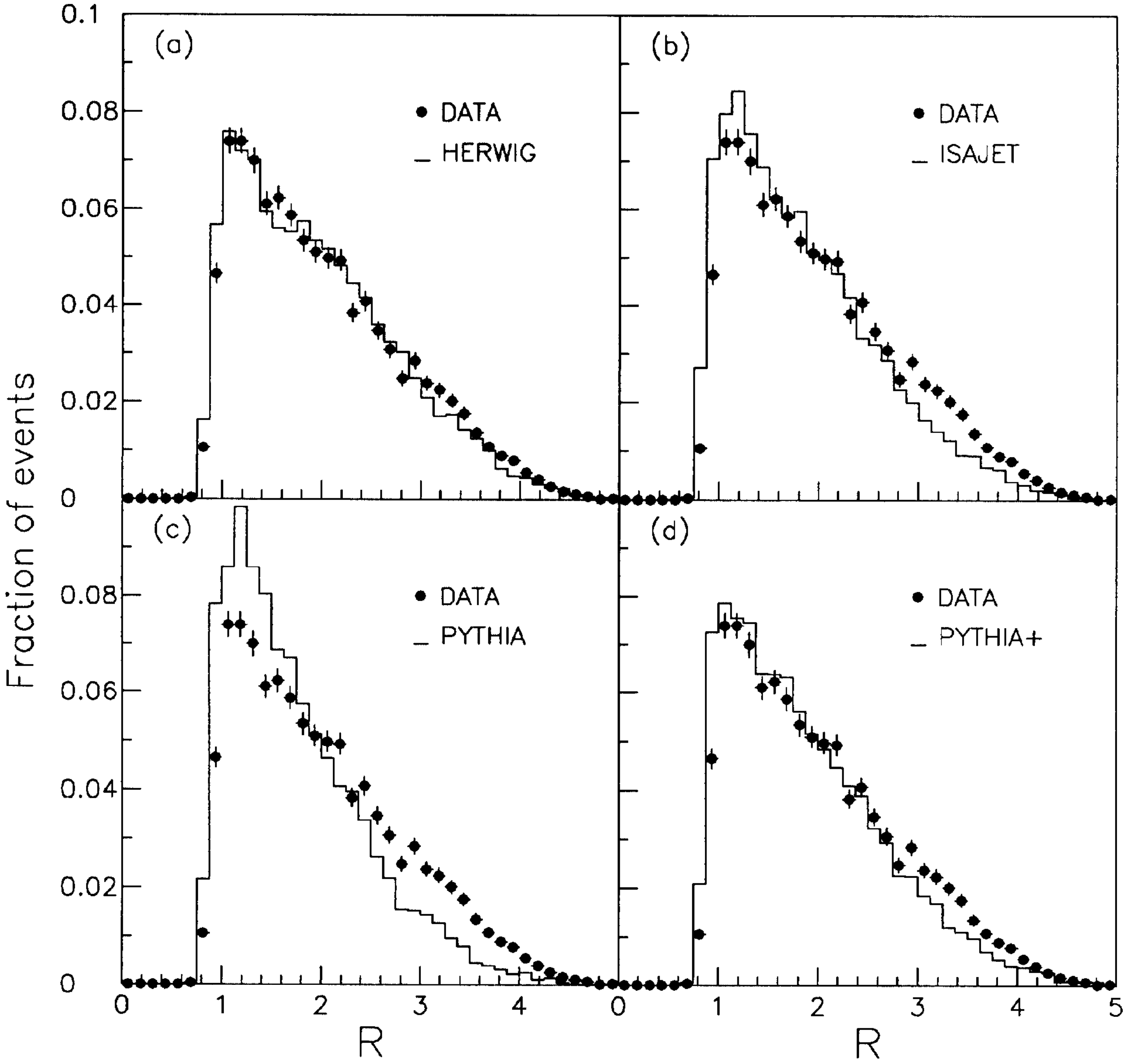

0.1
0.08
0.06
0.04
0.02
0
Fraction of events
(a)
● DATA
_ HERWIG
(b)
● DATA
_ ISAJET
(c)
● DATA
_ PYTHIA
(d)
● DATA
_ PYTHIA+
0
1
2
3
4
5
R
R

Figure 11:

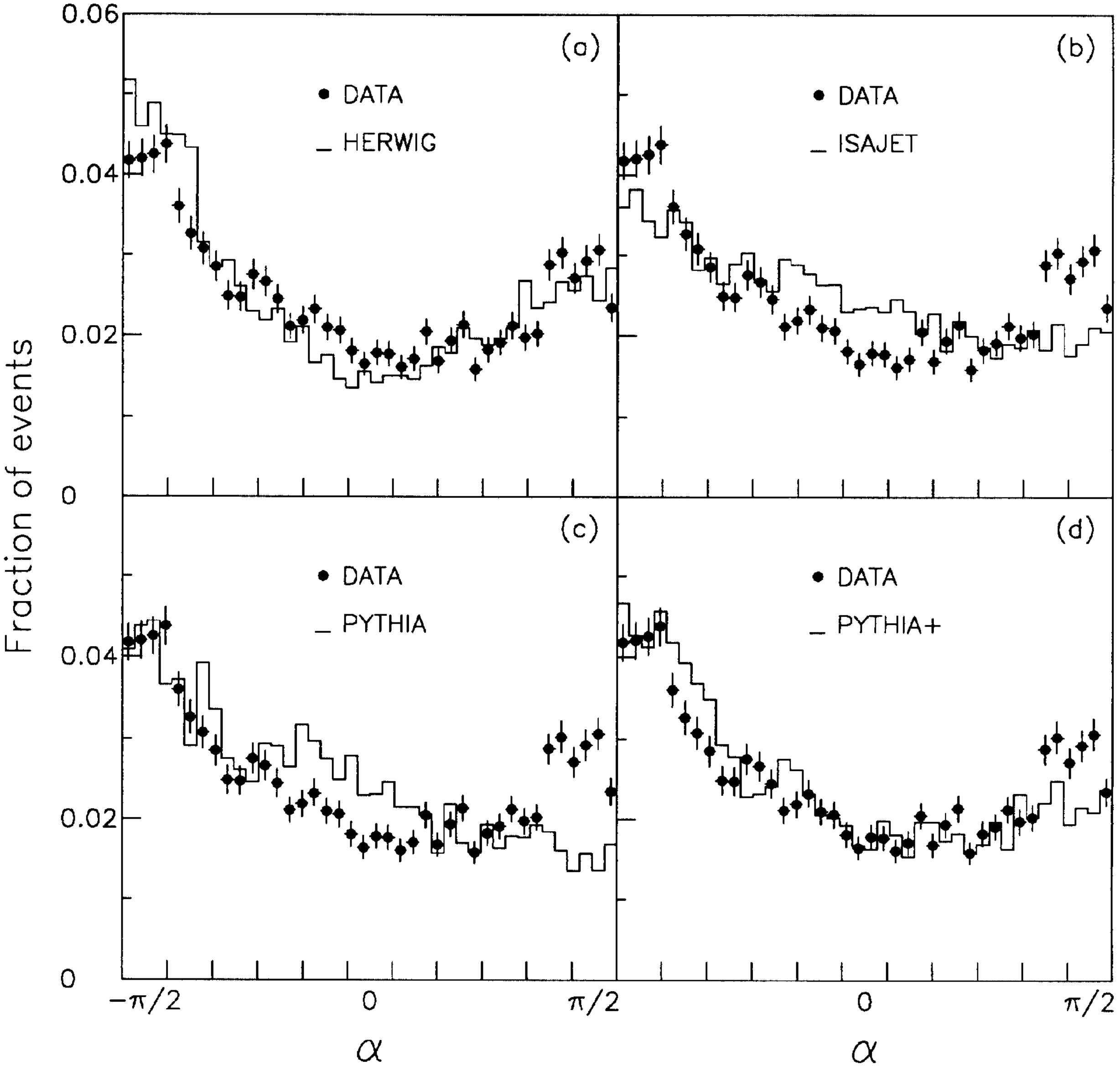

0.06
0.04
0.02
0
Fraction of events
(a)
● DATA
_ HERWIG
(b)
● DATA
_ ISAJET
(c)
● DATA
_ PYTHIA
(d)
● DATA
_ PYTHIA+
−π/2
0
π/2
α
0
π/2
α

Figure 12:

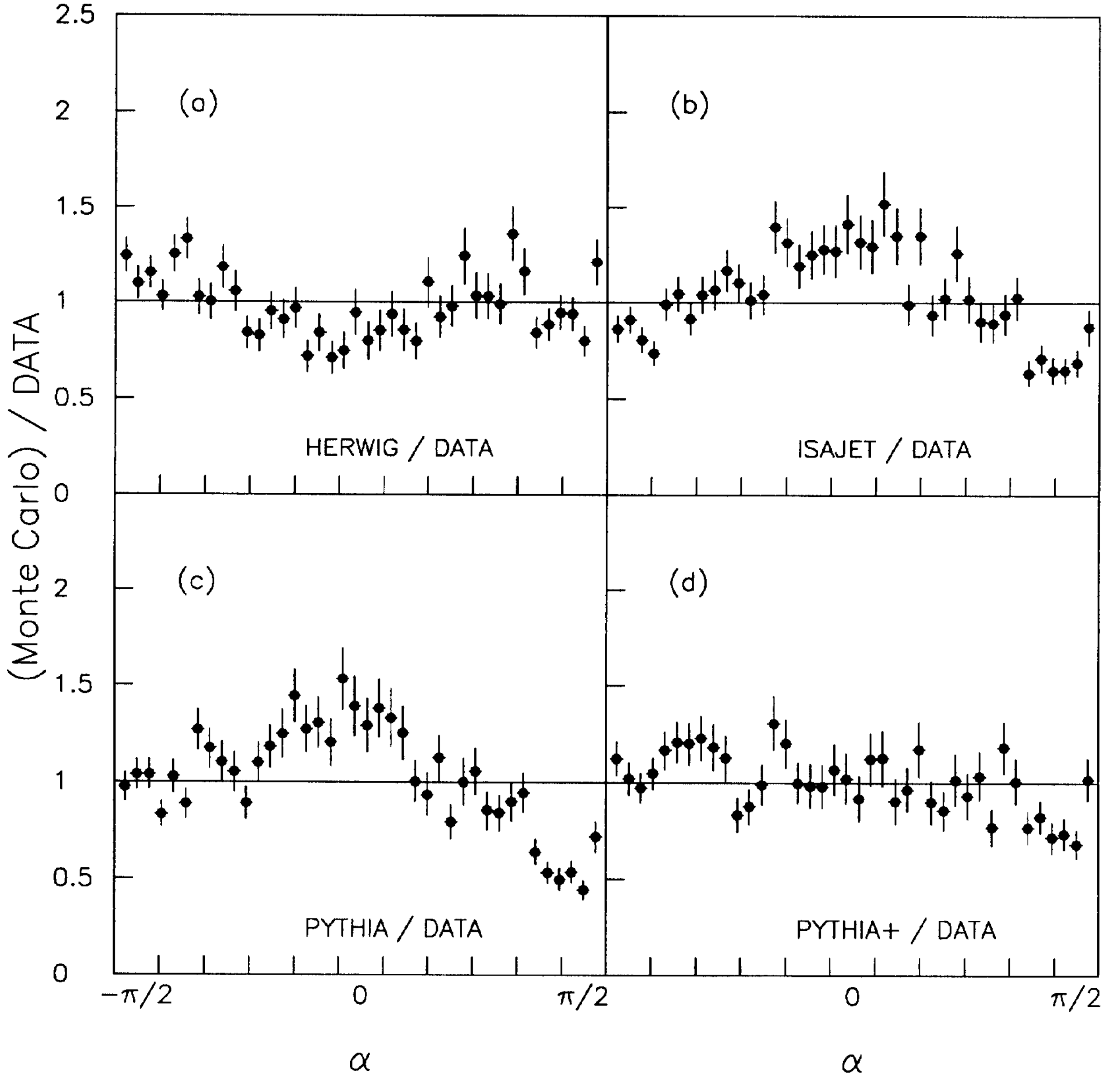
2.5
2
1.5
1
0.5
0
(a)
HERWIG / DATA
(b)
ISAJET / DATA
(c)
PYTHIA / DATA
(d)
PYTHIA+ / DATA
(Monte Carlo) / DATA
−π/2
0
π/2
α

Figure 13:

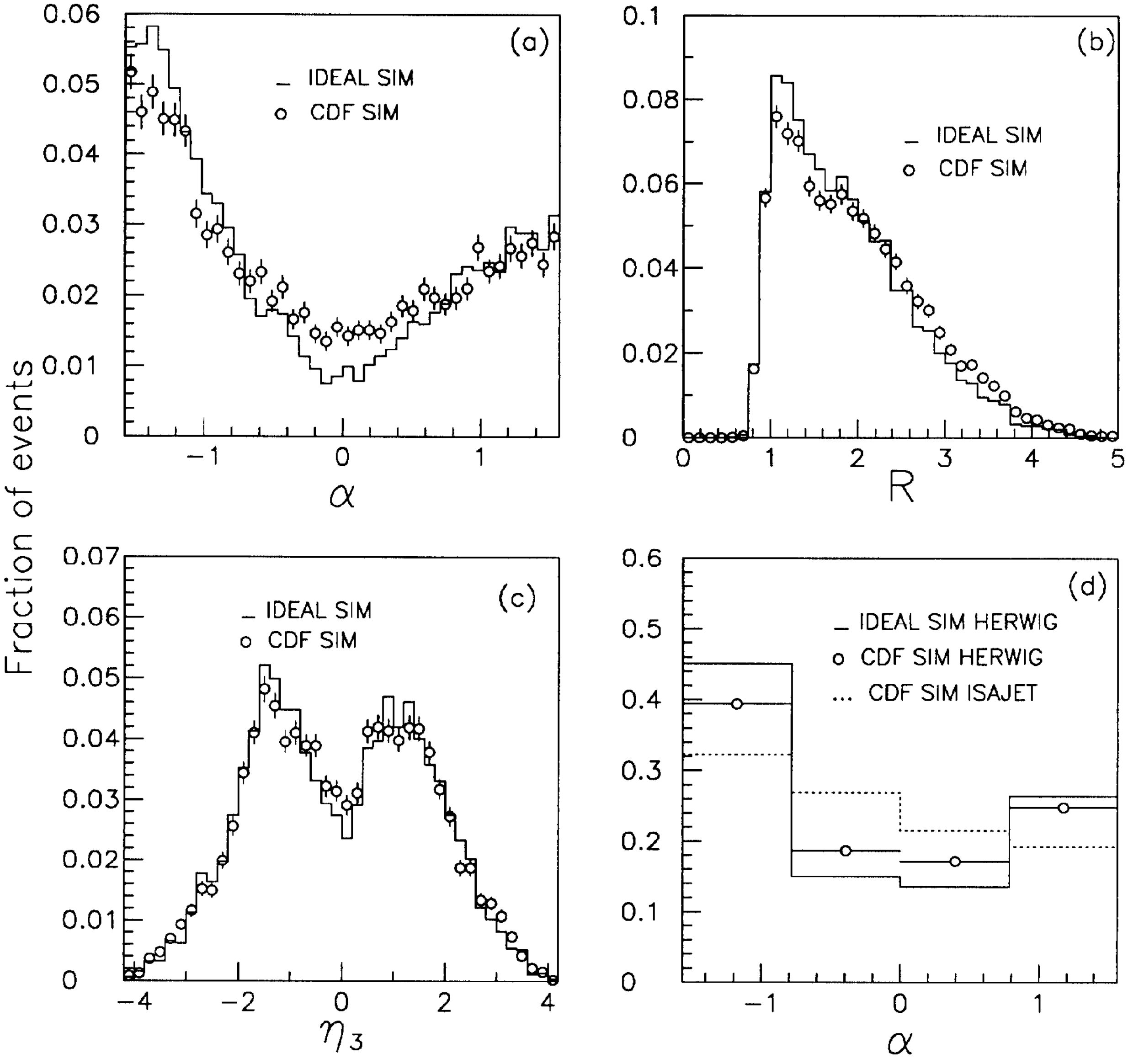

Fraction of events
(a)
IDEAL SIM
CDF SIM
0.06
0.05
0.04
0.03
0.02
0.01
0
−1
0
1
α
(b)
IDEAL SIM
CDF SIM
0.1
0.08
0.06
0.04
0.02
0
0
1
2
3
4
5
R
(c)
IDEAL SIM
CDF SIM
0.07
0.06
0.05
0.04
0.03
0.02
0.01
0
−4
−2
0
2
4
η_3
(d)
IDEAL SIM HERWIG
CDF SIM HERWIG
... CDF SIM ISAJET
0.6
0.5
0.4
0.3
0.2
0.1
0
−1
0
1
α

Figure 14:

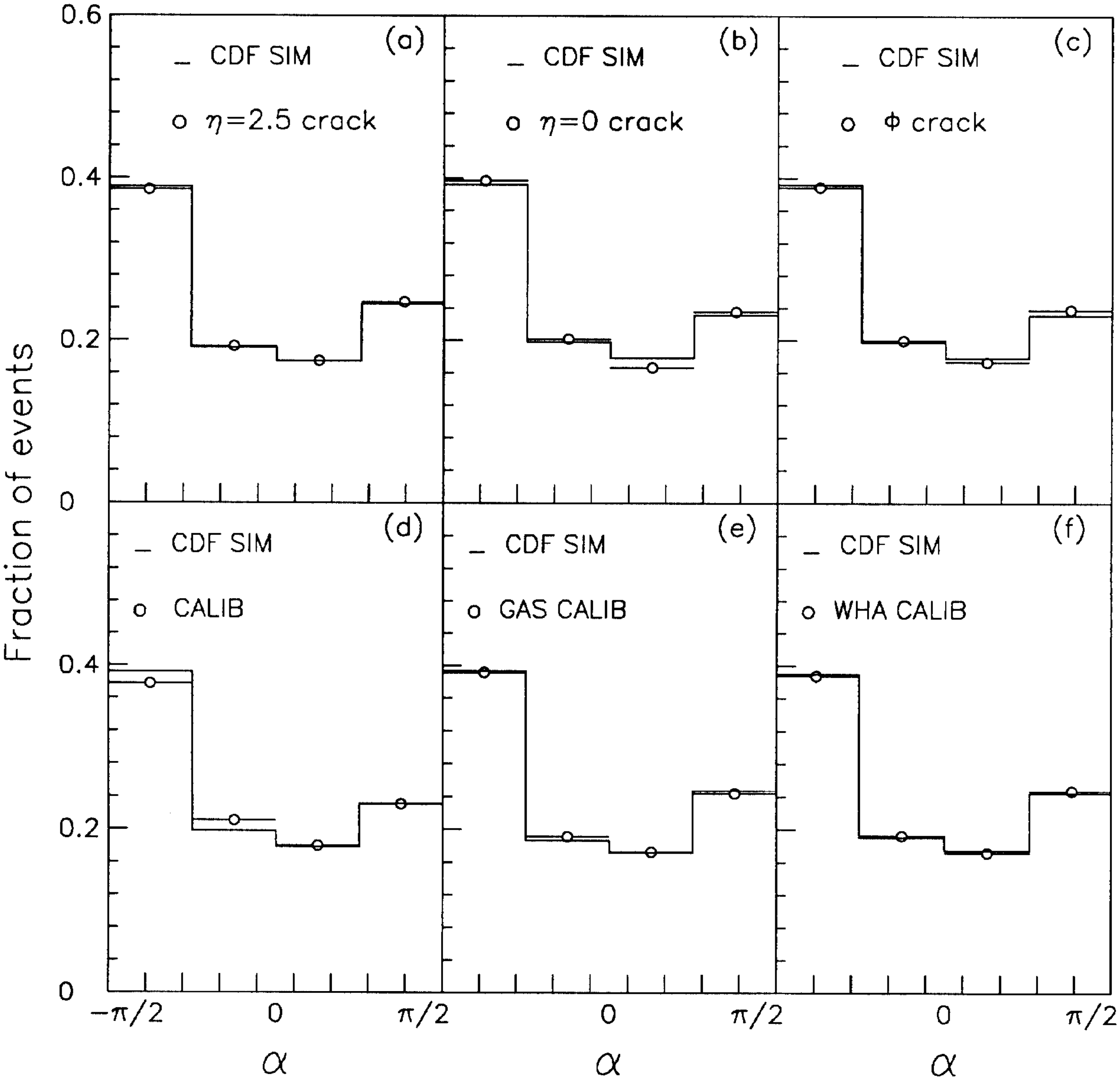

0.6
0.4
0.2
0
Fraction of events
(a)
_ CDF SIM
o η=2.5 crack
(b)
_ CDF SIM
o η=0 crack
(c)
_ CDF SIM
o Φ crack
(d)
_ CDF SIM
o CALIB
(e)
_ CDF SIM
o GAS CALIB
(f)
_ CDF SIM
o WHA CALIB
$-\pi/2$
0
$\pi/2$
α

Figure 15:

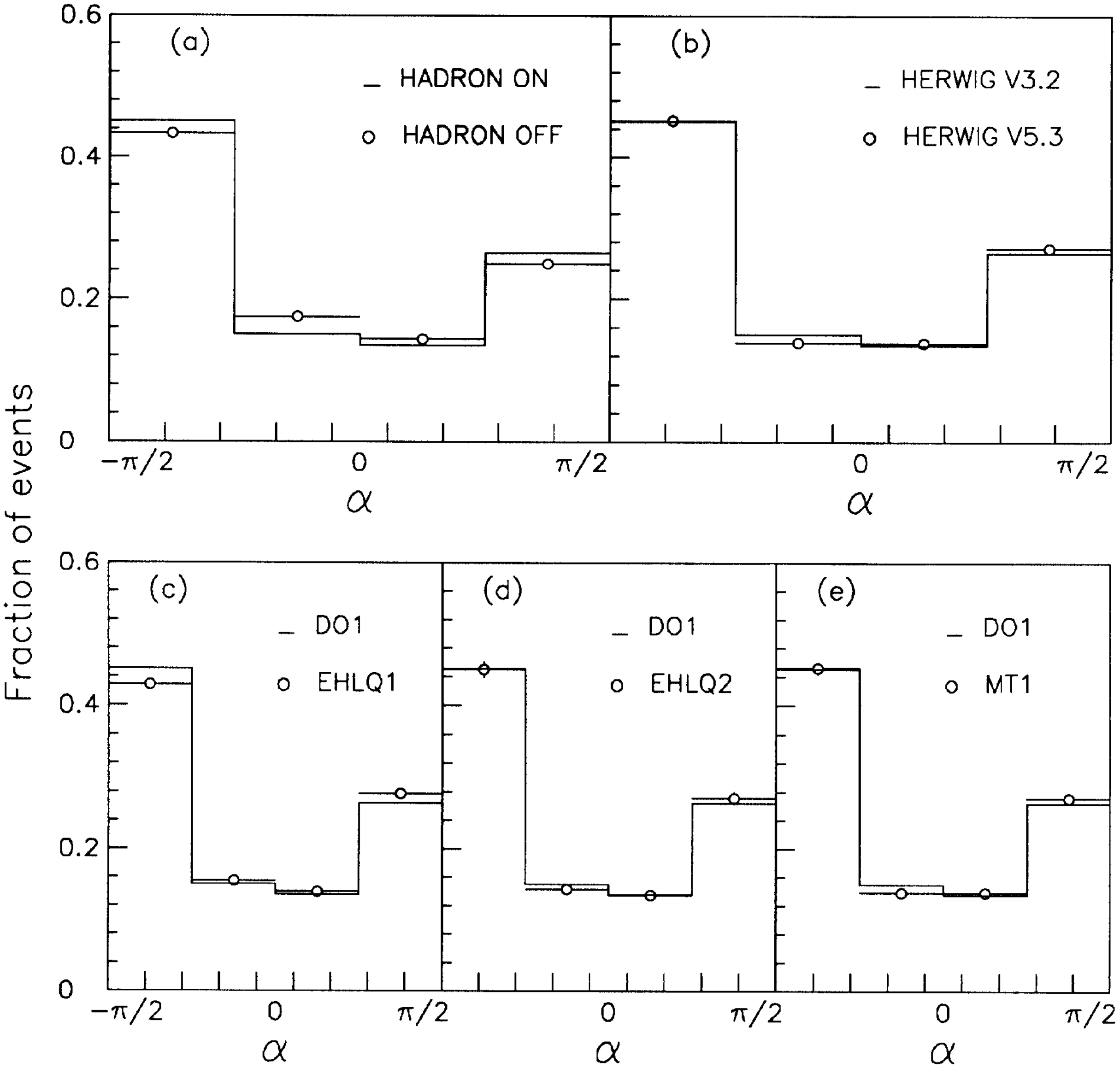
Fraction of events
0.6
0.4
0.2
0
(a)
_ HADRON ON
o HADRON OFF
(b)
_ HERWIG V3.2
o HERWIG V5.3
−π/2
0
π/2
α
(c)
_ DO1
o EHLQ1
(d)
_ DO1
o EHLQ2
(e)
_ DO1
o MT1

Figure 16:

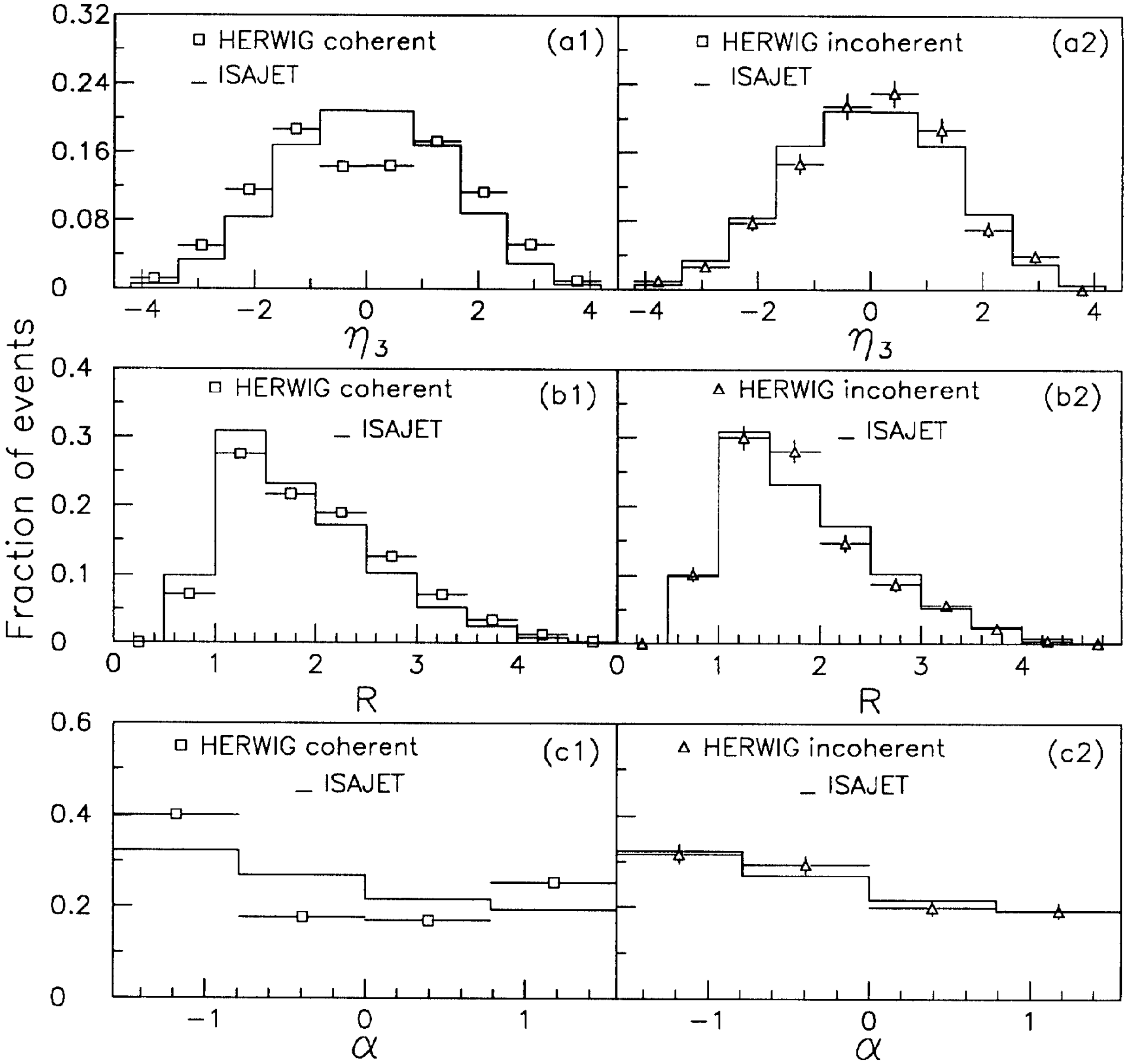
Fraction of events
□ HERWIG coherent
_ ISAJET
(a1)
□ HERWIG incoherent
_ ISAJET
(a2)
0.32
0.24
0.16
0.08
0
−4
−2
0
2
4
η_3
0.4
0.3
0.2
0.1
□ HERWIG coherent
_ ISAJET
(b1)
△ HERWIG incoherent
_ ISAJET
(b2)
R
0.6
0.4
0.2
□ HERWIG coherent
_ ISAJET
(c1)
△ HERWIG incoherent
_ ISAJET
(c2)
−1
1
α

Figure 17:

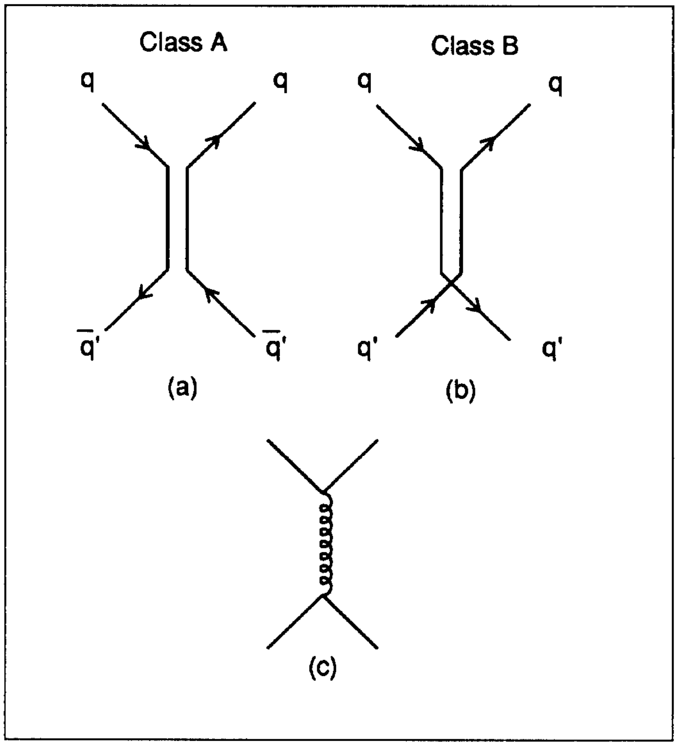

Figure 18:

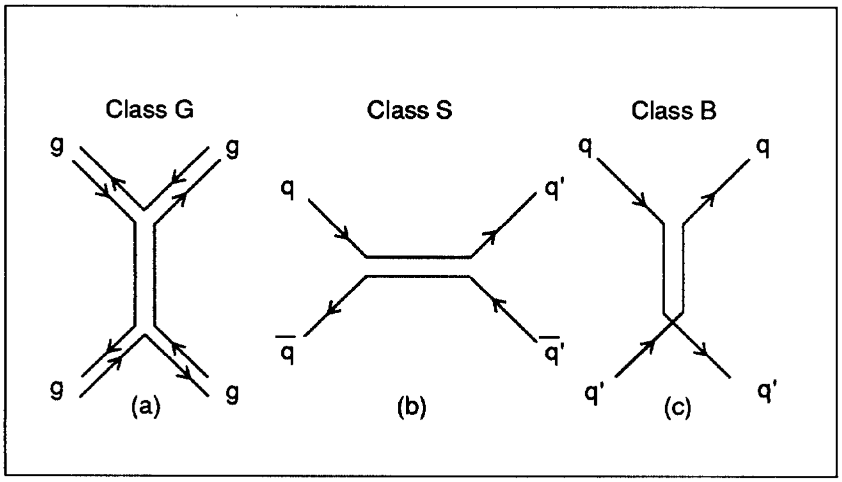

Figure 19:

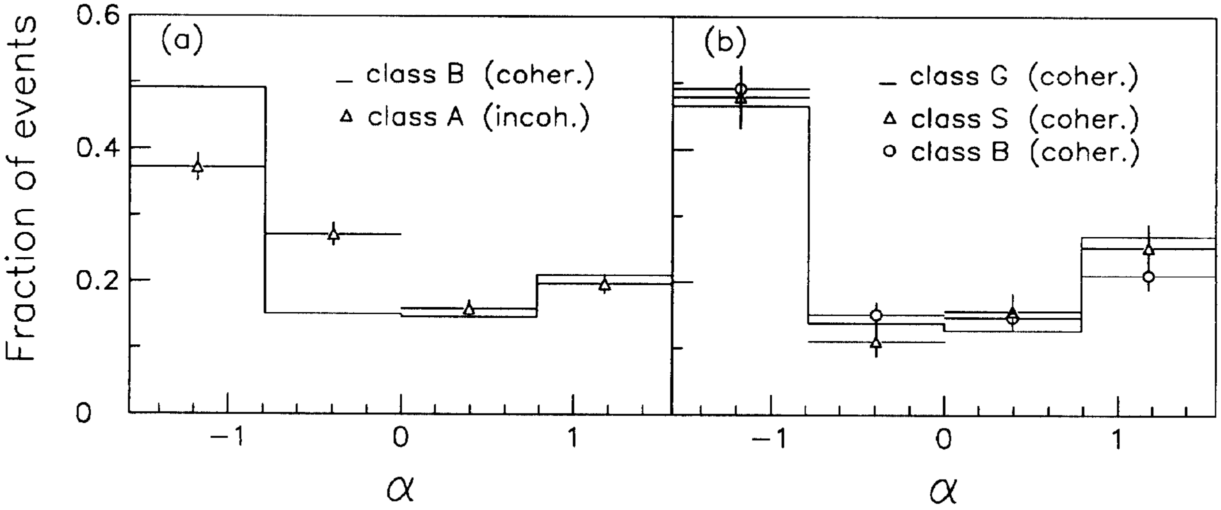
Fraction of events
0.6
0.4
0.2
0
(a)
_ class B (coher.)
Δ class A (incoh.)
−1
0
1
α
(b)
_ class G (coher.)
Δ class S (coher.)
○ class B (coher.)
−1
0
1
α

Figure 20:

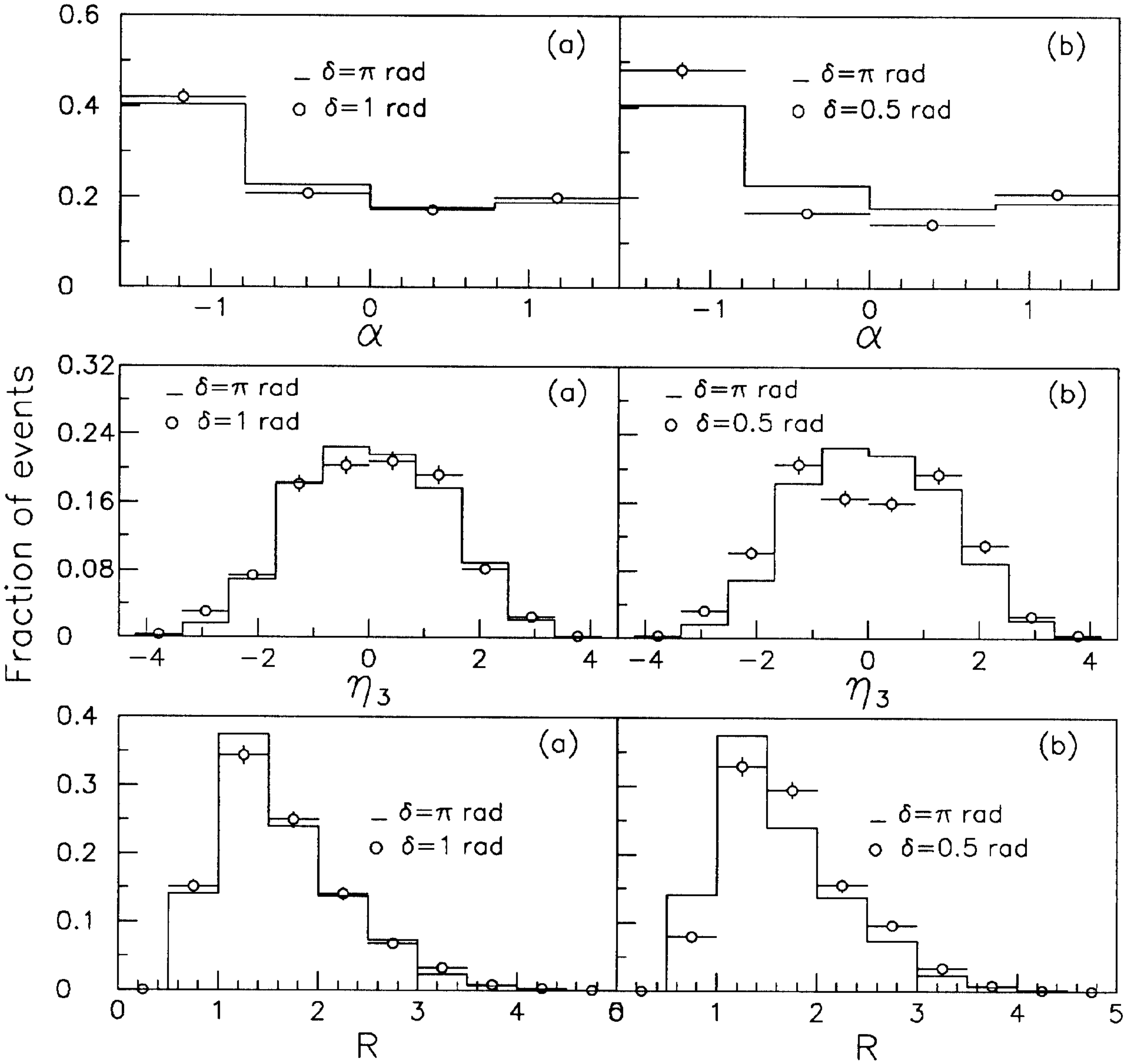
Fraction of events
0.6
0.4
0.2
0
(a)
_ δ=π rad
o δ=1 rad
(b)
_ δ=π rad
o δ=0.5 rad
−1
0
1
α
0.32
0.24
0.16
0.08
0
−4
−2
0
2
4
η3
0.4
0.3
0.2
0.1
0
1
2
3
4
5
R

Figure 21:

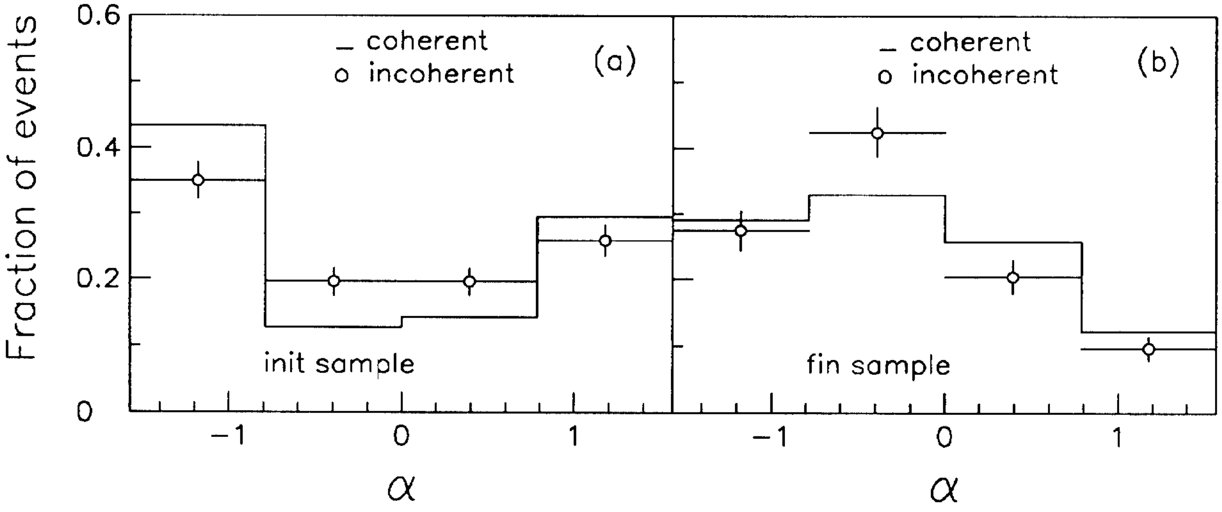
Fraction of events
0.6
0.4
0.2
0
_ coherent
o incoherent
(a)
init sample
−1
0
1
α
_ coherent
o incoherent
(b)
fin sample
−1
0
1
α

Figure 22:

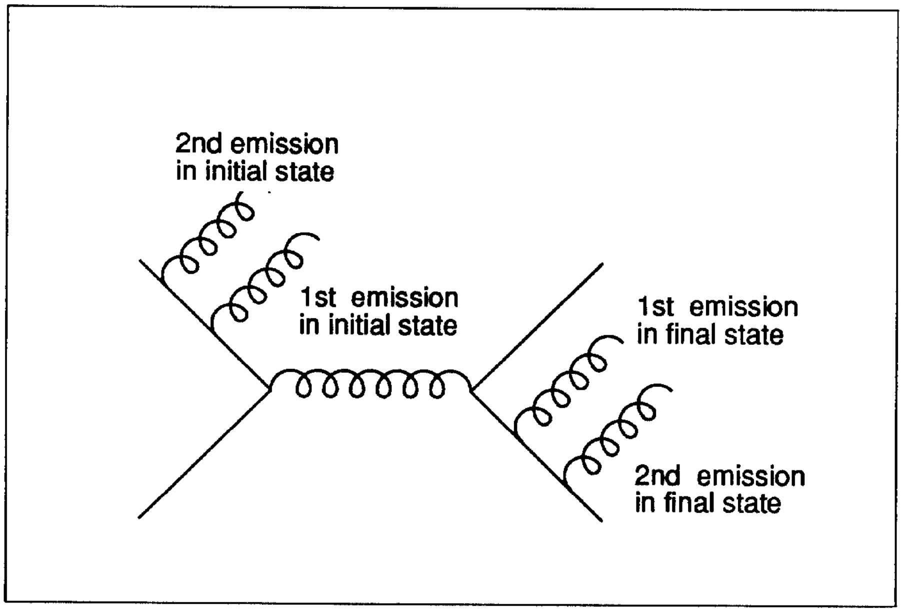

Figure 23:

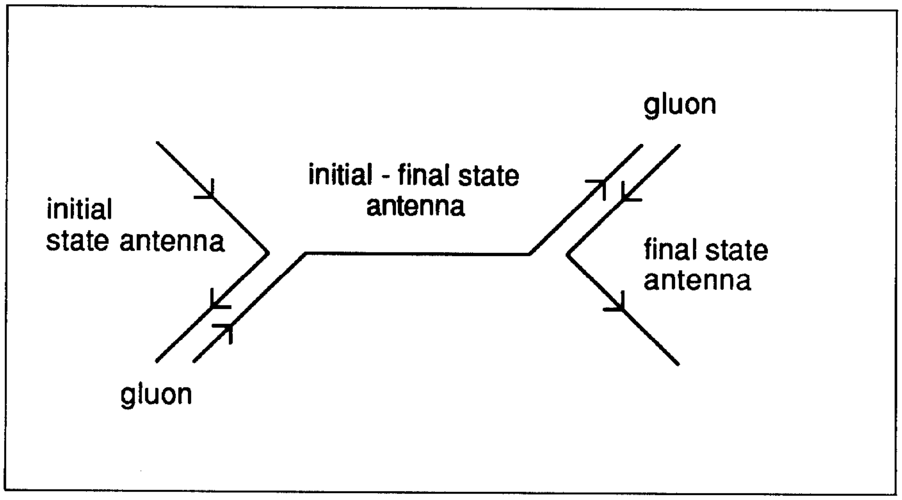

Figure 24:

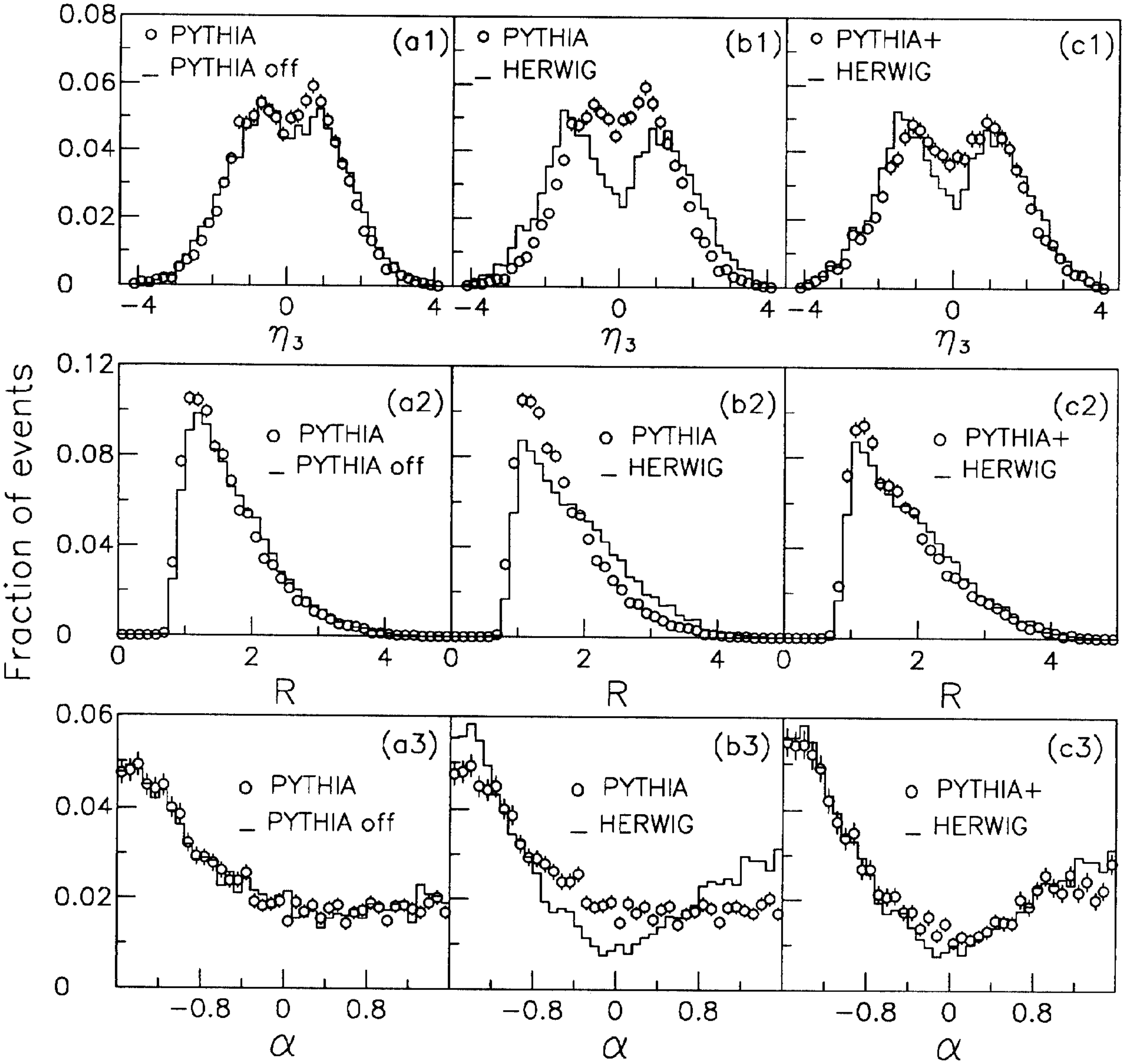
Fraction of events
0.08
0.06
0.04
0.02
0
o PYTHIA
_ PYTHIA off
(a1)
o PYTHIA
_ HERWIG
(b1)
o PYTHIA+
_ HERWIG
(c1)
−4
0
4
η_3
0.12
0.08
0.04
0
(a2)
(b2)
(c2)
0
2
4
R
0.06
0.04
0.02
0
(a3)
(b3)
(c3)
−0.8
0
0.8
α

Figure 25:

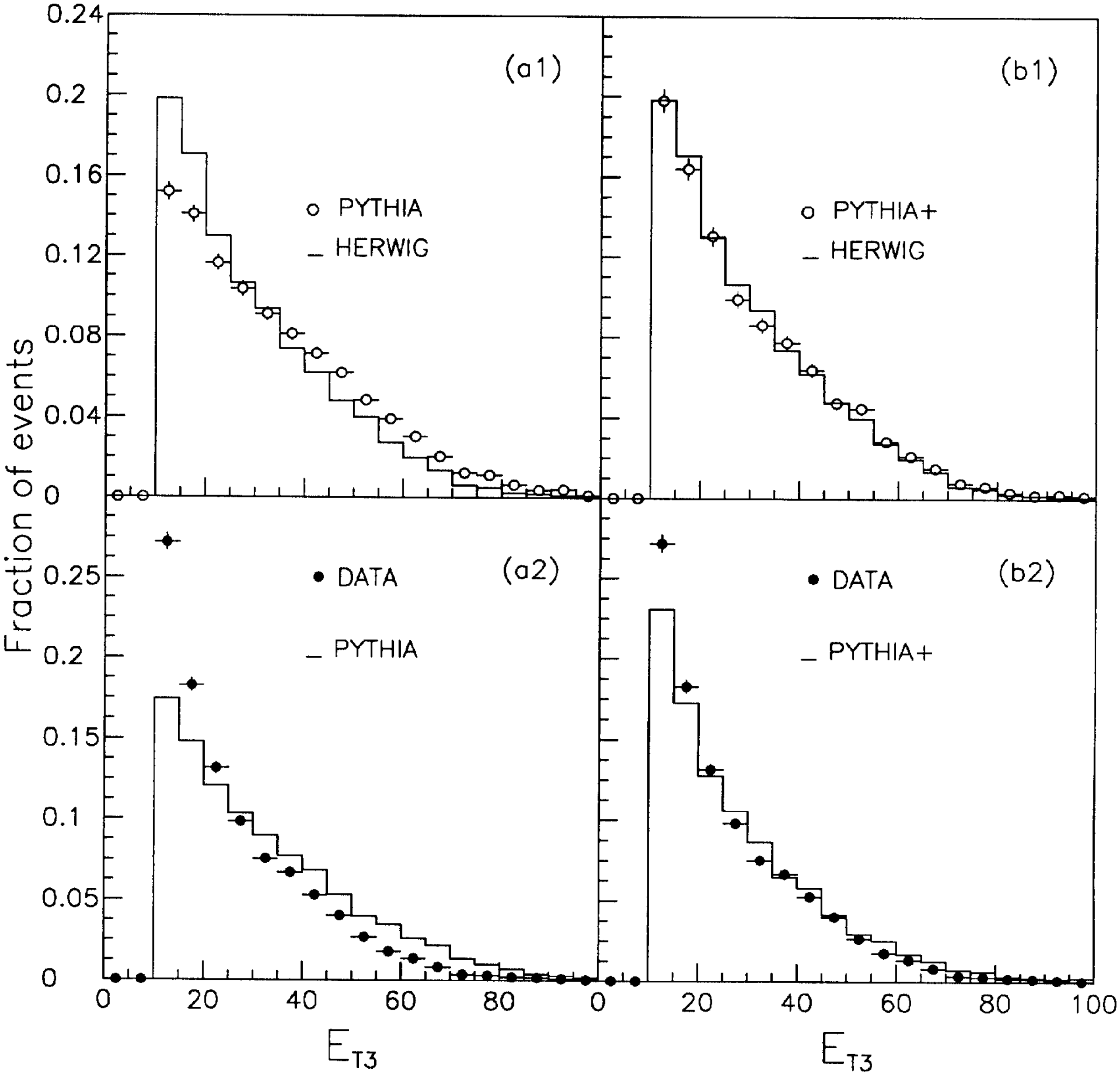
Fraction of events
0.24
0.2
0.16
0.12
0.08
0.04
0
0.25
0.2
0.15
0.1
0.05
0
(a1)
○ PYTHIA
_ HERWIG
(b1)
○ PYTHIA+
_ HERWIG
(a2)
● DATA
_ PYTHIA
(b2)
● DATA
_ PYTHIA+
0
20
40
60
80
0
20
40
60
80
100
E_{T3}
E_{T3}

Figure 26:

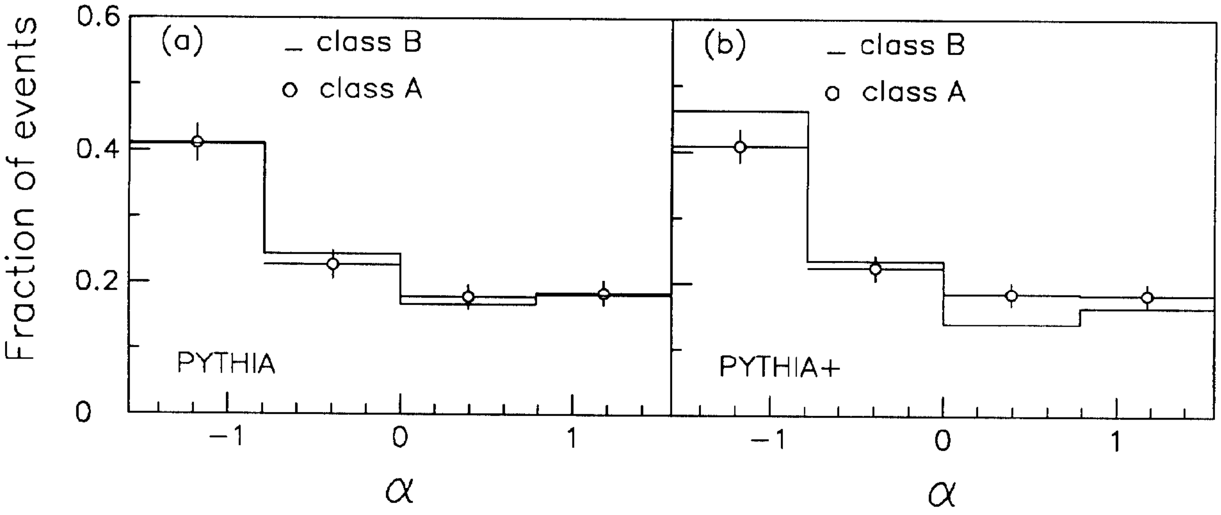
Fraction of events
0.6
0.4
0.2
0
(a)
_ class B
o class A
PYTHIA
−1
0
1
α
(b)
_ class B
o class A
PYTHIA+
−1
0
1
α

Figure 27:

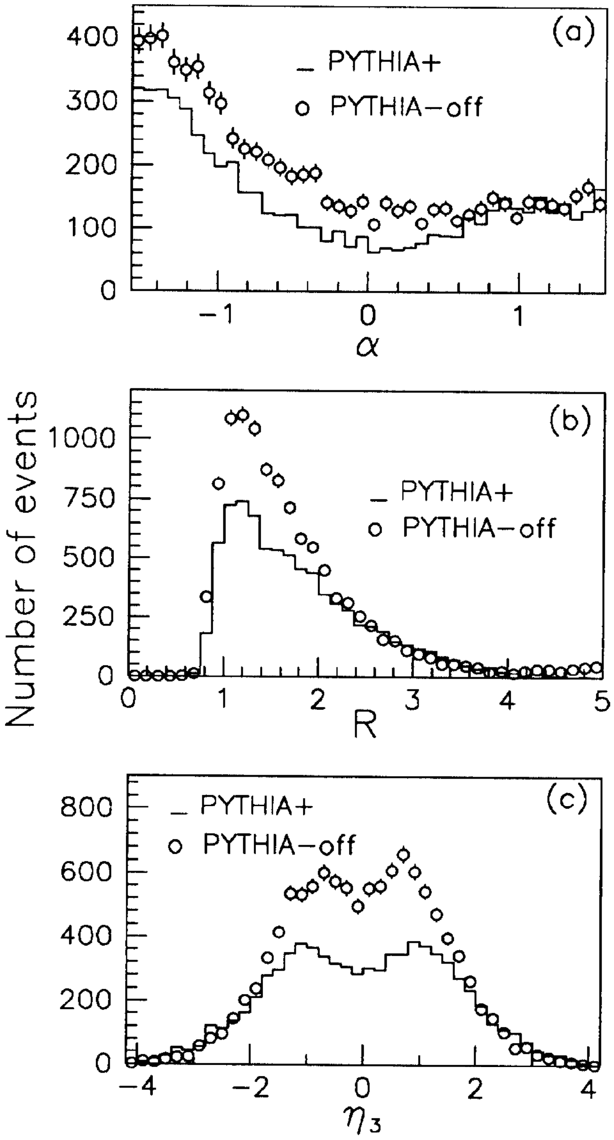

(a)
PYTHIA+
PYTHIA−off
400
300
200
100
0
−1
0
1
α
Number of events
(b)
PYTHIA+
PYTHIA−off
1000
750
500
250
0
0
1
2
3
4
5
R
(c)
PYTHIA+
PYTHIA−off
800
600
400
200
0
−4
−2
0
2
4
η_3

Figure 28: